ADVANCED FUNCTIONAL MATERIALS
www.afm-journal.de

Photocrosslinked Silk Fibroin Microgel Scaffolds for Biomedical Applications

Fatemeh Karimi, Nona Farbehi, Farzaneh Ziaee, Kieran Lau, Marzieh Monfared, Marija Kordanovski, Habib Joukhdar, Thomas G. Molly, Robert Nordon, Kristopher A. Kilian, Martina H. Stenzel, Khoon S. Lim, and Jelena Rnjak-Kovacina**

Silk fibroin hydrogels are extensively explored for tissue engineering and regenerative medicine as an artificial extracellular matrix (ECM) that can support tissue growth. However, the nanometer pore size of hydrogels limits adequate cell, tissue, and vascular infiltration. Microgel scaffolds are an emerging class of microporous biomaterials formed by annealing small microscale hydrogels (microgels) into a 3D construct. In this work, silk microgels are generated using a microfluidic device that allows tuning of the microgel diameter (100–400 µm) and are stabilized via visible light-initiated photo-crosslinking of native tyrosine residues in silk. Microgels are then covalently annealed using silk solution as glue and the same cytocompatible visible light-initiated crosslinking to form microgel scaffolds. Unlike the nano-porosity of bulk photo-crosslinked silk hydrogels, the microgel scaffolds have an average pore diameter of 29 ± 17 or 192 ± 81 µm depending on the microgel size, with enhanced mechanical properties compared to bulk hydrogels. This microporosity supports enhanced cell spreading and proliferation in vitro and increases scaffold remodeling in vivo, encouraging improved tissue infiltration and matrix deposition. The microgel size and material format also affect inflammatory responses in vivo. This work demonstrates that silk microgels and microgel scaffolds are promising candidates for tissue engineering and regenerative medicine applications.

1. Introduction

Engineered polymeric hydrogels are widely researched and utilized as medical devices, artificial matrices for cell and tissue culture, biosensors, and drug delivery systems.[1–3] Traditional bulk hydrogels have nano-scale pores that permit the diffusion of small molecules but limit cell and vascular infiltration, properties essential for successful tissue integration and regeneration post-implantation.[4] Various processing techniques have been utilized to introduce micro-scale porosity into bulk hydrogels, with most focusing on sacrificial templating, where ice crystals, salt, or polymers are introduced into the hydrogel network and removed to leave behind micro-scale pores.[5,6] However, the harsh nature of these processing methods often makes them incompatible with the encapsulation of cells and the inclusion of growth factors in the hydrogels. Alternatively, biodegradable crosslinks have been incorporated into hydrogels to allow protease-based degradation and cellular

F. Karimi, N. Farbehi, F. Ziaee, K. Lau, M. Kordanovski, H. Joukhdar, R. Nordon, J. Rnjak-Kovacina
Graduate School of Biomedical Engineering
University of New South Wales
Sydney, NSW 2052, Australia
E-mail: fatemeh.karimi@unsw.edu.au; j.rnjak-kovacina@unsw.edu.au

N. Farbehi
Garvan Weizmann Center for Cellular Genomics
Garvan Institute of Medical Research
Sydney, NSW 2010, Australia

The ORCID identification number(s) for the author(s) of this article can be found under https://doi.org/10.1002/adfm.202313354

DOI: 10.1002/adfm.202313354

K. Lau, K. S. Lim
School of Medical Sciences
Faculty of Medicine and Health
University of Sydney
Sydney, NSW 2006, Australia

M. Monfared, M. H. Stenzel
Centre for Advanced Macromolecular Design
School of Chemistry
University of New South Wales
Sydney, NSW 2052, Australia

T. G. Molly, K. A. Kilian
School of Materials Science and Engineering
University of New South Wales
Sydney, NSW 2052, Australia

T. G. Molly
Department of Bioengineering
University of California San Diego
La Jolla, CA 92093, USA

infiltration over time. However, fine-tuning hydrogel degradation is difficult and often results in either hydrogel loss before tissue repair or slow degradation that results in fibrotic encapsulation.[7,8] Rapid hydrogel degradation can also compromise the mechanical stability and utility of hydrogels. Thus, despite the recent progress in hydrogel materials and technologies, nano-scale pores of traditional bulk hydrogels can limit their widespread success in tissue engineering and regenerative medicine applications.

An alternative approach to the traditional bulk hydrogels is engineering hydrogels with suitable micron-sized pores where the path for the cellular infiltration is not contingent on hydrogel degradation, as was recently demonstrated via annealed microgel scaffolds.[4,9] Microgels are hydrogel microparticles that can be fabricated into a variety of shapes and sizes (≈1–1000 µm) using techniques such as batch emulsions, microfluidics, electrodynamic spraying, and lithography.[4] Microgels have unique properties compared to traditional bulk hydrogels, including shear-thinning behavior that permits injection through small gauge needles and tunable properties that allow for the mixing of multiple microgel populations with varying composition, size, and content to create tailored materials. Recently, microgels have been engineered into annealed microgel scaffolds where the microgel building blocks are imperfectly annealed to one another via functional groups on the microgel surface to generate scaffolds with interconnected micropores that can be easily traversed by infiltrating cells. The porosity of microgel scaffolds can be tuned by the size and packing density of microgels.[4,10] The advantage of this system is that cell loading and pore formation within scaffolds can occur simultaneously by mixing cells with microgel building blocks prior to annealing. To date, microgel annealed scaffolds have been generated from synthetic and natural polymers including polyethylene glycol (PEG),[11,12] hyaluronic acid,[9,13–17] chitosan,[18] and gelatin,[19] and have been annealed using a range of chemistries including carbodiimide,[17,19] enzymatic (human factor XIII)),[9,15,17] photo-initiated (via Eosin Y),[17] tetrazine-norbornene click,[13,16] and copper-free azide-alkyne reactions,[12] as well as electrostatic,[18] and guest-host molecular interactions.[11,14] Microporous microgel scaffolds have been used successfully for cell encapsulation,[20] delivery of growth factors,[18] tissue repair,[21] wounding healing,[9] and regeneration of neural,[15,18] and cardiac tissue.[14,22]

Bombyx mori silk fibroin (referred to as silk throughout)-based biomaterials have been explored extensively for tissue engineering and regenerative medicine applications due to their tunable physicochemical properties, excellent cytocompatibility, low inflammatory profile, and excellent mechanical properties.[23,24] Traditionally, bulk silk hydrogels have been formed via physical crosslinking by inducing β-sheets in the aqueous silk solution through sonication, electrical current, modulation of pH, or addition of alcohol.[25,26] β-sheet-stabilized silk microgels have also been also fabricated via batch emulsion,[27] microfluidic devices,[28] solvent coagulation,[29] and high-voltage electrostatic field.[30] These microgels have been used for growth factor[30] and drug[27,28] delivery and for tissue regeneration.[28,29] Silk microgel scaffolds with high compression modulus (≈18 MPa) have been fabricated by annealing silk microgels using silk solution and β-sheet formation (physical crosslinking) for bone regeneration applications.[29] However, the physically crosslinked silk microgels are typically brittle and are not easily remodeled by cells due to their highly crystalline and nano-porous nature.[31,32] In addition, encapsulation of cells within these hydrogels or scaffolds is limited due to the harsh nature of the fabrication process, typically involving alcohols, sonication, or drastic pH changes. In recent years, covalent di-tyrosine bond formation between silk polymer chains has gained popularity as an alternative cytocompatible approach to silk hydrogel formation, providing crosslinking in the absence of β-sheet formation and effective cellular encapsulation during hydrogel formation.[33,34] Formation of covalent di-tyrosine crosslinks in silk can be induced by a range of approaches, including enzymatic,[35,36] Fenton,[37,38] and photo-initiated reactions.[34,39–43] The use of photo-initiated crosslinking has the advantage of the rapid and controlled formation of hydrogels with tunable stiffness and compatibility with various biofabrication approaches[26,34,39–43] and due to the abundance of tyrosines in native silk, the reaction can occur without the need to modify silk with additional reactive moieties. One of the most popular approaches to photo-initiated crosslinking of unmodified silk to form di-tyrosine bonds involves the photo-initiator ruthenium(II) hexahydrate (Ru(II)(bpy)32+) (Ru) and sodium persulphate (SPS) as the electron acceptor. Photocrosslinking using this method results in rapid silk gelation (<1 min) into optically transparent gels that support high-density encapsulation of cells.[34] This method also supports simple and effective biofunctionalization of silk biomaterials with bioactive molecules, and in the case of proteins, supports covalent crosslinks between the protein of interest and silk while maintaining protein bioactivity.[34,44] While the utility of phot-crosslinking has been demonstrated in generating bulk hydrogels and silk biofabrication, to the best of our knowledge, the photo-crosslinking method has not been used for the formation of silk microgels or annealed microgel scaffolds for tissue engineering and regenerative medicine applications.

In this study, we have developed the first microporous silk microgel scaffolds using di-tyrosine crosslinking via visible light-initiated chemistry. This system has two unique advantages, including (i) the formation of covalently crosslinked silk microgels without the need to chemically modify silk polymer or to add additional functional groups and (ii) the use of silk solution as a glue to anneal microgels together and engineer microporous microgel scaffolds using tsimple and cytocompatible visible light-initiated crosslinking method. Microporous silk microgel scaffolds composed of either small or large microgels were generated and their properties were compared with traditional bulk silk hydrogels in terms of morphology, mechanical properties, handling, cell encapsulation, and tissue interactions in vivo. The unique properties of this fabrication approach and the resultant tunable

K. S. Lim
Department of Orthopaedic Surgery and Musculoskeletal Medicine
University of Otago Christchurch
Christchurch 8011, New Zealand
J. Rnjak-Kovacina
Tyree Foundation Institute of Health Engineering
University of New South Wales
Sydney, NSW 2052, Australia

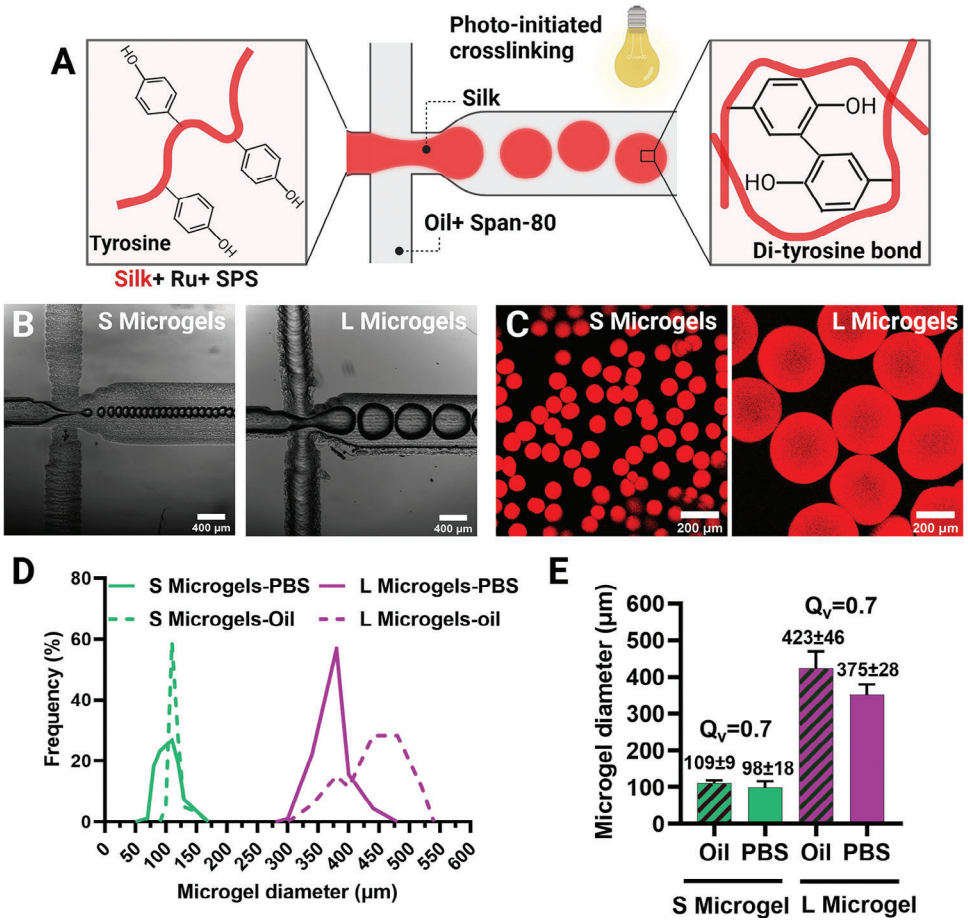

Figure 1. Silk microgel formation. A) Schematic representation of silk microgel formation in a microfluidic device and crosslinking through di-tyrosine formation via the Ru/SPS photo-initiated reaction. B) Small (S) and large (L) microgel formation in the microfluidic device. Scale bars are 400 µm. C) Fluorescently labeled S and L microgels. Scale bars are 200 µm. D) Size distribution of small and large microgels in oil and PBS. E) Average diameter and the volumetric swelling ratio (Q_v) of S and L microgels after collection in oil (pre-swelling) and after washing and storage in PBS (post-swelling). Data are mean ± SD, $N = 53–82$.

material platform will find a wide range of applications in the field of biomaterials, tissue engineering, and regenerative medicine.

2. Results and Discussion

2.1. Silk Microgel Preparation and Characterization

Silk microgels were fabricated using a water-in-oil emulsion approach within a flow-focusing microfluidic device made from polydimethyl siloxane (PDMS) (**Figure** 1A; Figures S1–S3, Supporting Information). A schematic representation of the microfluidic device and the production of microgels are shown in Figure 1A. One aqueous stream of silk hydrogel precursor solution (3% w/v) containing the ruthenium (Ru) photo-catalyst and the sodium persulfate (SPS) initiator and one oil stream containing Span-80 were used. The microscale droplets of silk were formed by pinching the silk aqueous stream by the oil stream and were stabilized against coalescence by Span-80 surfactant before crosslinking. Two sizes of silk droplets (small and large) were produced using microfluidic devices with two different channel sizes as shown in Figure 1B. Apart from the channel size, the size of silk droplets was also controlled by regulating the flow rate of oil to the aqueous phase. The collected microscale silk droplets were exposed to a visible light source to stabilize the shape of silk microgels through the crosslinking of silk polymer chains by the formation of di-tyrosine crosslinks initiated by Ru/SPS (Figure 1A; Figure S4, Supporting Information). Silk fibroin contains tyrosine residues (≈5% of all amino acid residues)[23] in its polymer chain which enables radical coupling of phenol moieties without further modification of the polymer chain.[34] The high efficiency and rapid reactivity of Ru/SPS-based photo-initiated system allowed for the quick formation of stable silk microgels. In addition, this system provides the ability to produce stable and elastic microgels in one step without any further processing such as vacuum or alcohols which are necessary for the stabilization of microgels made by the traditional physical β-sheet crosslinking.[28,29]

The microgels were stabilized via photo-crosslinking in oil and then washed with PBS multiple times to remove oil residues and surfactant. While the di-tyrosine crosslinking of bulk silk hydrogels using Ru/SPS is well established in the literature,[33,34]

we have also confirmed the presence of the typical fluorescence of di-tyrosine bonds when excited under UV light, which is not observed in uncrosslinked silk (Figure S5A, Supporting Information). The collected and isolated silk microgels were imaged and their diameter was measured (Figure 1C; Figure S6, Supporting Information). The size range and the average size of microgels after stabilization in oil and after washing in PBS are shown in Figure 1D and E, respectively. The small and large microgels demonstrated an average diameter of 109 ± 9 and 423 ± 46 µm in oil (pre-swelling), respectively, which was slightly reduced to 98 ± 18 and 375 ± 28 µm after washing in PBS (post-swelling). The use of microfluidic devices generated microgels with a narrow size distribution in oil which did not change by changing the environment to PBS due to the homogenous swelling process. The volumetric swelling ratio of microgels (Q_v) was determined as 0.7 for both small and large microgels, demonstrating a slight reduction in their size after changing their environment into PBS possibly due to the rearranging of the silk polymer chains.

2.2. Formation of Microporous Silk Microgel Scaffolds

Small or large silk microgels were annealed to one another to form microporous microgel scaffolds. A schematic representation of scaffold formation is presented in **Figure 2A**. Silk solution (3% w/v) was used to anneal the silk microgels together via light-mediated crosslinking of di-tyrosine bonds between the tyrosine residues of the silk polymer solution and the remaining tyrosine residues on the surface of silk microgels. In the absence of the silk solution or photo-initiator, the microgels did not anneal to form a scaffold (data not shown). The advantage of this system is the use of the same polymer for microgel formation and as a glue to anneal microgels, paired with the use of cytocompatible Ru/SPS and visible light crosslinking system,[34] allowing cell encapsulation during scaffold formation. It is worth mentioning that the silk solution has previously been used to anneal microgels made from PEG or silk (crosslinked by β-sheets) using crosslinking driven by β-sheet formation; however, this physical β-sheet based crosslinking process is not compatible with cell encapsulation and scaffolds lacked microporosity.[29,45] We have confirmed that the microgel annealing in our system is not due to the spontaneous formation of β-sheets between the microgels, as the microgel scaffolds remain intact when incubated in lithium bromide under the conditions used to disrupt β-sheets and resolubilize native silk fibers[46] (Figure S5B,C, Supporting Information).

A syringe was used to template cylindrical microgel scaffolds as shown in Figure 2B. This provided an easy and accessible system for scaffold formation and transfer, a feature particularly useful during scaffold implantation in vivo. The annealed scaffolds were porous with interconnected pores (Figure 2C,D). Despite using Ru/SPS crosslinked silk as the "glue" in the interstitial space, we observed microporosity between the microgels, with only silk fibers observed between individual microgels (Figure 2C). We hypothesize that this is due to the absorption of the silk solution into the microgel surface, thus facilitating bond formation between microgels without obstructing pores between them, as well as likely less efficient crosslinking of silk between microgels (Figure S10B,C, Supporting Information). Due to the random settling/packing of the microgels, a range of pore sizes was achieved (Figure 2E). With an increase in the size of microgel building blocks from 98 µm (small) to 375 µm (large), the average pore diameters increased from 29 ± 17 to 192 ± 81 µm (Figure 2F), demonstrating tunability. To demonstrate pore interconnectivity and void fraction of the silk microgel scaffolds, small and large microgel scaffolds were incubated with a high molecular weight FITC-dextran (150 kDa) which can diffuse the scaffold's micron-sized pores but not the nanopores of the microgel building blocks (Figure 2G). Increasing microgel size correlated with an increase in the microgel scaffold void fraction (Figure 2H). Together, these data highlight that silk-annealed microgel scaffolds with interconnected and micro-scale pores can be formed by annealing the silk microgels of varying sizes using di-tyrosine crosslinking. In addition, the high porosity of scaffolds compared to bulk hydrogels is expected to provide a faster mass transfer rate and more opportunity for cell-material interactions and infiltration which is necessary for maintaining cell viability, tissue engineering, and tissue regeneration.[4,9]

2.3. Tunability of Microporous Silk Microgel Scaffolds

One of the key advantages of microporous microgel scaffolds is the ability to mix multiple microgel populations of varying compositions or loaded with different cargo. Thus, in order to demonstrate the tunability of our system, two different types of fluorescent-tagged bovine serum albumin (BSA) were used as model cargo to encapsulate within the silk microgels during their fabrication. Fluorescent-tagged BSA was successfully loaded in the silk microgels as expected. One type of microgels was prepared with BSA-Alexa fluor 594 conjugate (red) and the other with BSA-Alexa fluor 488 conjugate (green) (**Figure 3A**). After fabrication, different ratios of green and red microgels were mixed together in order to generate microgel scaffolds with different compositions of green or red BSA (Figure 3A). Depending on the blending ratios, we were able to control the distribution of the loaded cargo in the final microgel scaffolds as confirmed by confocal images (Figure 3B). This demonstrates a simple fabrication approach to generate microporous scaffolds with a highly tunable distribution of cell binding or signaling molecules; a feature that is difficult to achieve in the more traditional microporous scaffolds generated via sacrificial templating approaches, or in bulk hydrogels. Additionally, like BSA, any proteins with tyrosine residues can be covalently immobilized in the microgels, allowing them to remain stable in the microgel scaffolds for prolonged periods of time.[44,47]

Therefore, this system allows microgel building blocks loaded with a variety of molecules such as cell binding moieties, drugs, cytokines, and growth factors to be mixed in different ratios to build highly tunable microporous scaffolds. The properties of each microgel population can be controlled individually without impacting the total properties of the microgel scaffold. For example, microgels with different shapes, sizes, or crosslinking densities can be prepared to control the release rate of the loaded molecules, thus allowing both spatial and temporal control over their delivery, making this a robust biomaterial platform.

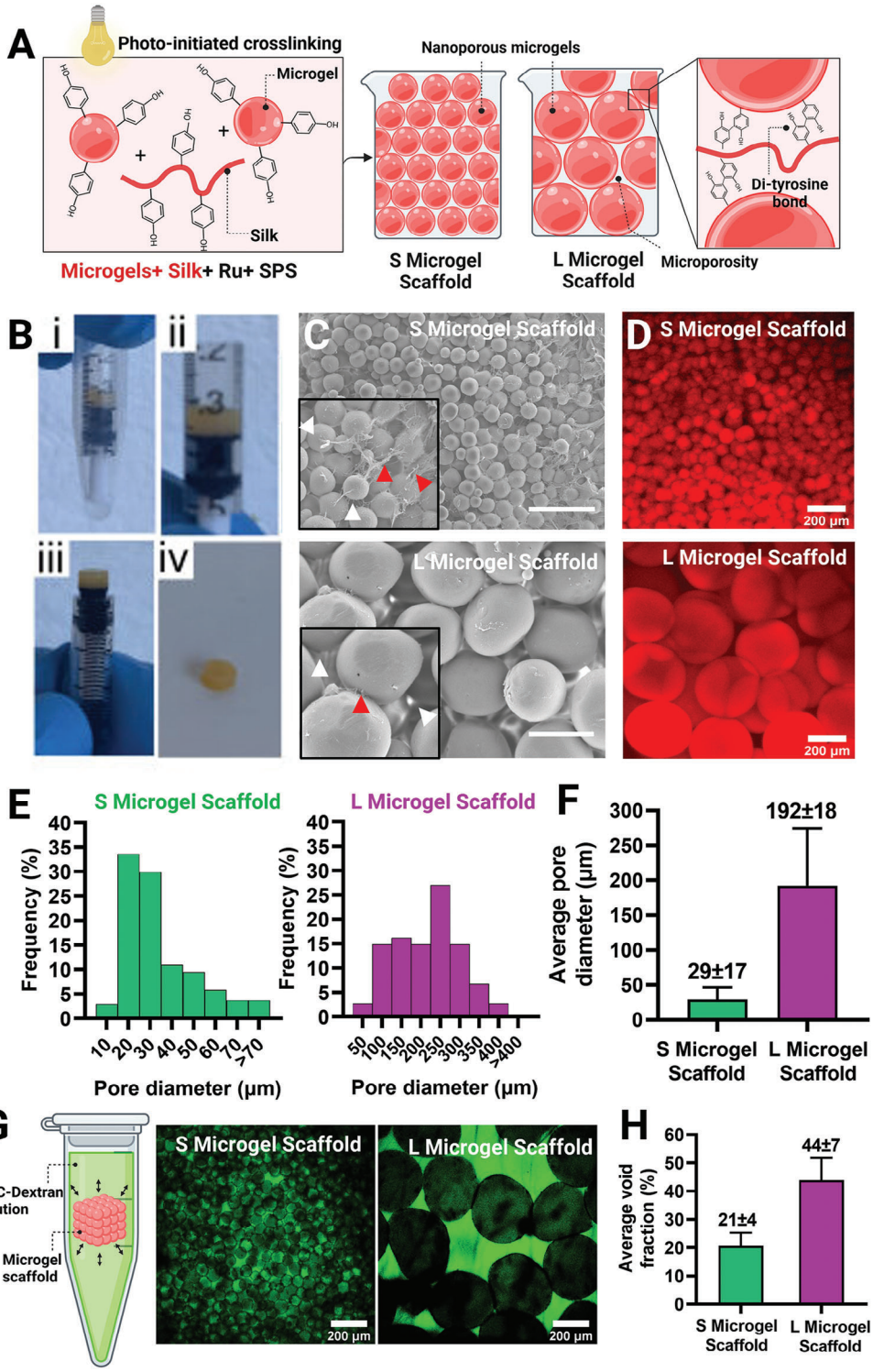

Figure 2. Fabrication of small (S) and large (L)microporous silk microgel scaffolds. A) Schematic representation of S and L microporous silk microgel scaffold formation via Ru/SPS photo-initiated crosslinking and using silk as a glue to anneal silk microgels. B) Formation of the cylindrical-shaped microgel scaffolds using a mold made from a syringe. C) SEM images of small and large microgel scaffolds. Scale bars are 250 µm. Insets show that silk glue forms a fibrous, non-continuous network between the microgels (red arrows), leaving open void spaces/pores between microgels (white arrows). D) Fluorescently labeled S and L microgel scaffolds. Scale bars are 200 µm. E) Pore diameter distribution in S and L microgel scaffolds. F) Average pore diameter of S and L microgel scaffolds. G) Schematic representation and confocal images of the diffusion of FITC-dextran solution (150 kDa) within the micron size pores of microgel scaffolds. Scale bars are 200 µm. H) Average void fraction percentage of S and L microgel scaffolds. Data are mean ± SD, $N = 74–137$ (E,F), and $N = 6$ (H).

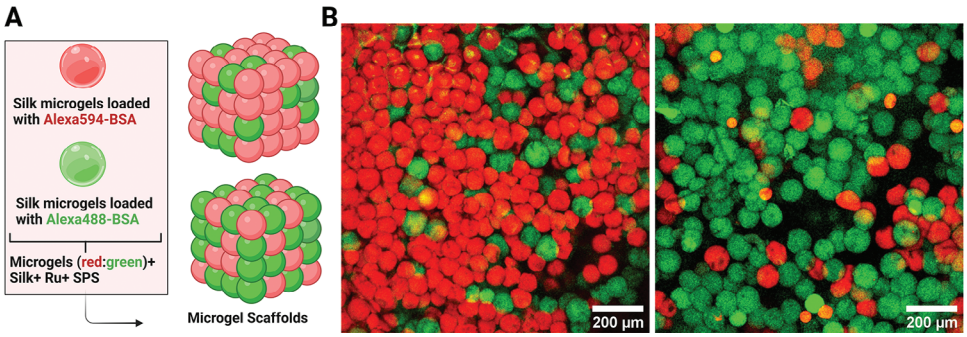

Figure 3. Fabrication of heterogenous microporous silk microgel scaffolds. A) Fabrication of small silk microgels by encapsulating BSA-Alexa fluor 594 conjugate (red) and BSA-Alexa fluor 488 conjugate (green) and fabrication of microporous silk microgel scaffolds by mixing different ratios of red and green small microgels (8:2 and 2:8 red to green in the top and bottom image, respectively). B) Confocal images of small microgel scaffolds generated by mixing different ratios of red and green silk microgels. Scale bars are 200 µm.

2.4. Comparison of the Swelling and Degradation Properties of Bulk Hydrogels and Microgel Scaffolds

The swelling ratio and degradation rate of small and large microgel scaffolds were measured and compared with traditional bulk silk hydrogels (**Figure 4**). No difference was observed between the swelling ratio of small microgel scaffolds and bulk hydrogels. However, large microgel scaffolds demonstrated a higher swelling ratio than the bulk hydrogel ($p < 0.01$) (Figure 4A). This can be explained by the two-scale matrix structure, consisting of the intraparticle crosslinked matrix of each individual microgel and the interparticle microporous matrix. While bulk hydrogel swelling is limited by the swelling capacity of their polymer matrix, the microgel scaffolds can swell further into the interstitial space of the packed microgels,[4] as observed with the large microgel scaffolds here.

Degradation of bulk silk hydrogels and microgel scaffolds was assessed using Protease XIV over 8 days (Figure 4B). Protease XIV is a cocktail of bacterial proteolytic enzymes, providing a useful analytical tool to compare the relative degradation rate of silk-based biomaterials in an accelerated in vitro degradation model.[48] Bulk hydrogel and microgel scaffolds both showed a low degree of mass loss in PBS within the first 2 days of incubation after which the mass remained stable. This initial mass loss in PBS is likely due to the loss of uncrosslinked silk polymer in the hydrogels and scaffolds. In Protease XIV, both small and large microgel scaffolds showed similar degradation rates (with almost complete degradation after 8 days) which was faster than the degradation rate of the bulk hydrogels (14% mass remained after 8 days) ($p<0.01$). The small and large microgel scaffolds have microporosity and high surface area that provide faster penetration and enhanced contact of the enzyme with the surface of microgels, resulting in an increased rate of microgel scaffold degradation. However, bulk hydrogels have nanoporosity and low surface area which limits the penetration rate of the enzyme within the hydrogels. Thus degradation likely occurs mostly through surface erosion and this reduces the degradation rate of the bulk hydrogels compared to microgel scaffolds. Therefore, the fabrication of microporous silk microgel scaffolds allows tuning of the material degradation not only via controlling the crosslinking density of the hydrogel or microgel but also via controlling the pore size of the scaffolds. This plays an important role in in vivo degradation of microgel scaffolds compared to bulk hydrogels.

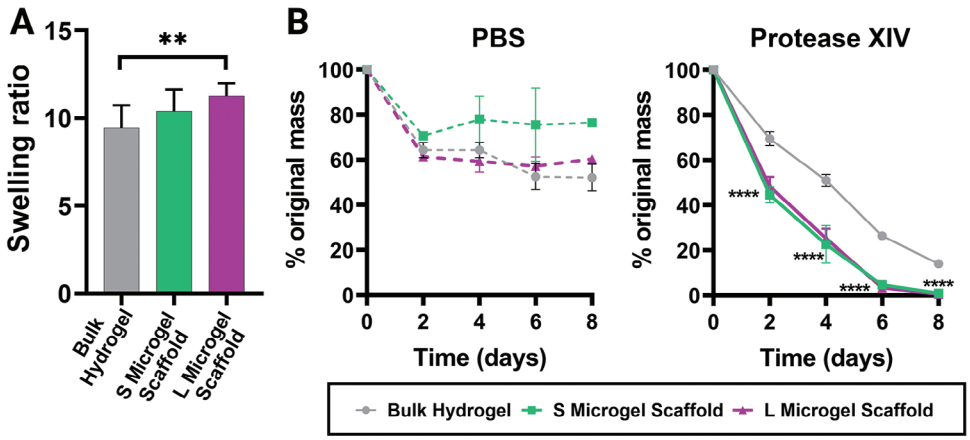

Figure 4. Swelling and degradation properties of bulk hydrogel and small (S) and large (L)microgel scaffolds. A) Swelling ratio of bulk hydrogel and S and L microgel scaffolds. B) Mass loss percentage of bulk hydrogel and S and L microgel scaffolds over 8 days in PBS and Protease XIV. Statistically significant differences indicated are relative to bulk hydrogel in Protease XIV. Data are mean ± SD, $N = 5$.

2.5. Mechanical Properties of Bulk Hydrogels, Microgels, and Microgel Scaffolds

Jammed microgel suspensions have distinct viscoelastic properties that are useful for the injection of these materials. These properties include shear thinning, where the viscosity of the solution drops with increased force and shear rate, and having a critical yield stress, where a threshold of force must be surpassed to induce flow. Therefore, rheological analysis was performed to confirm these behaviors in the small and large microgels before annealing (**Figure 5**A,B; Figure S8, Supporting Information). Both the small and large microgel suspensions behaved as solids until yielding at 1.1 kPa (1.6% strain) and 1.7 kPa (2.2% strain) of stress, respectively (Figure 5A). A strain rate sweep (0.01–10 1 s^{-1}) confirmed that both microgel suspensions are shear thinning and able to flow at high applied shear rates (Figure S8A, Supporting Information). Cyclic strain sweeps of high and low shear strains demonstrated that the small and large microgels can self-heal and recover once the high shear strain is removed (Figure 5B). Here, when high force was applied quickly, the silk microgel suspension underwent a rapid transition to a liquid-like state before subsequently reverting to a solid-like state once the force was released. It is important to note that both small and large silk microgels exhibited ≈1000 times higher storage moduli and viscosities (Figure 5B; Figure S8, Supporting Information) than other non-annealed microgels used as injectables.[9,17] This may be due to the higher stiffness of the individual silk microgels fabricated in this study (shown in Figure 5G) compared to PEG, hyaluronic acid, or gelatin microgels with lower stiffness.[9,11,12,14,15,19] This shows that silk microgels have the correct rheological behavior required for an injectable jammed suspension. Previous work has demonstrated the tunability of the Ru/SPS-based crosslinking of silk, allowing control over the mechanical properties of silk hydrogels[34] suggesting that the mechanical properties and rheological behavior of silk microgels can be tuned with the right combination of silk concentration and crosslinking density to engineer injectable suspensions and printable materials for a variety of applications.

To investigate the mechanical properties of microgel suspensions post-annealing (i.e., microporous microgel scaffolds), compression tests were performed on cylindrical bulk hydrogels and microgel scaffolds (Figure 5C–F). The bulk hydrogels and small and large microgel scaffolds had a compressive modulus of 52 ± 5, 18 ± 5, and 44 ± 10 kPa, respectively (Figure 5D). No difference was observed between the compressive modulus of bulk hydrogel and the large microgel scaffold; however, both showed higher compressive modulus than the small microgel scaffold ($p < 0.05$). The high compressive modulus of the bulk hydrogel can be attributed to its homogeneity, allowing it to uniformly distribute stress during compression. The comparatively high modulus of the large microgel scaffolds demonstrates that the large microgels are strongly annealed together, suggesting that the incorporation of large micron-scale pores within the scaffold has little impact on the scaffold's compressive modulus. However, when microgel size was reduced, pore sizes were reduced and a significant reduction in the compressive modulus was observed. This indicates that the scaffold's compressive modulus (or stiffness) can be modulated by varying the size of microgels. Both small and large microgel scaffolds were significantly softer than microgel scaffolds made using β-sheet crosslinked silk microgels (3% silk, ≈503 µm diameter individual microgels, scaffold compressive modulus ≈18 MPa),[29] demonstrating that the di-tyrosine crosslinking supports the formation of softer materials and tunable mechanical properties via control over individual microgel properties and their annealing into microgel scaffolds. Bulk hydrogel and microgel scaffolds showed similar yield stress but different deformation strain ($p < 0.05$) (Figure 5E,F). Interestingly, the yield strain of the bulk hydrogels was 71%, lower than that of the small (76%) and large (84%) microgel scaffolds (Figure 5F). This is likely due to the microgels shifting and filling the void spaces as the scaffolds are compressed, allowing higher compression strains, less material deformation, and the ability to return to their original state post-compression. This was further illustrated when both small and large microgel scaffolds were manually handled; microgel scaffolds were compressed between two fingers (to half their height) and then released (Figure S9, Supporting Information). As shown in Figure S9 (Supporting Information), the microgel scaffolds maintained their original height once released. Interestingly, SEM images (Figure S10, Supporting Information) taken after the compression test show that microgels maintained their original morphology following compression, while bulk hydrogels ruptured and deformed. This demonstrates that the microgels are robust and can endure high forces and implies that even in an environment where they are subjected to the high sheer rates within a syringe or needle, these microgels will not burst and most likely will maintain their structure. These data along with the rheological data demonstrate the ability of both small and large microgel scaffolds to be handled and resist deformation.

Microgel suspensions are complex composite materials with the mechanics of individual particles that can differ from the properties of the bulk jammed suspension. These local properties are particularly important to study as cells constantly sense their local mechanical microenvironment and this plays a large role in directing cell behavior. As such, bulk rheology and macroscale compression tests are insufficient to properly characterize the entire mechanical landscape seen by individual cells. AFM-based nanoindentation analysis was performed on individual particles (Figure 5G). No difference was observed between the mean modulus of bulk hydrogels and both the small and large microgels (≈150 kPa). Combining these data with the compression results suggests that the elastic modulus of the microgel scaffolds can be controlled independently from the stiffness of individual microgels. Notably, the local stiffness of silk microgels prepared in this study is significantly higher than the local stiffness observed for other microgels made from natural polymers such as hyaluronic acid (with a local stiffness of ≈800 Pa),[17] likely due to the high strength and stiffness of silk polymers. These unique and tunable mechanical properties make silk microgels an important addition to the microgel biomaterial landscape.

2.6. Cellular Interactions with Microgel Scaffolds

To assess cell interactions with bulk and microporous silk hydrogels, human dermal fibroblast cells were encapsulated by mixing the cells with hydrogel precursor or microgel building blocks followed by crosslinking (**Figure 6**A). This allowed for the uniform

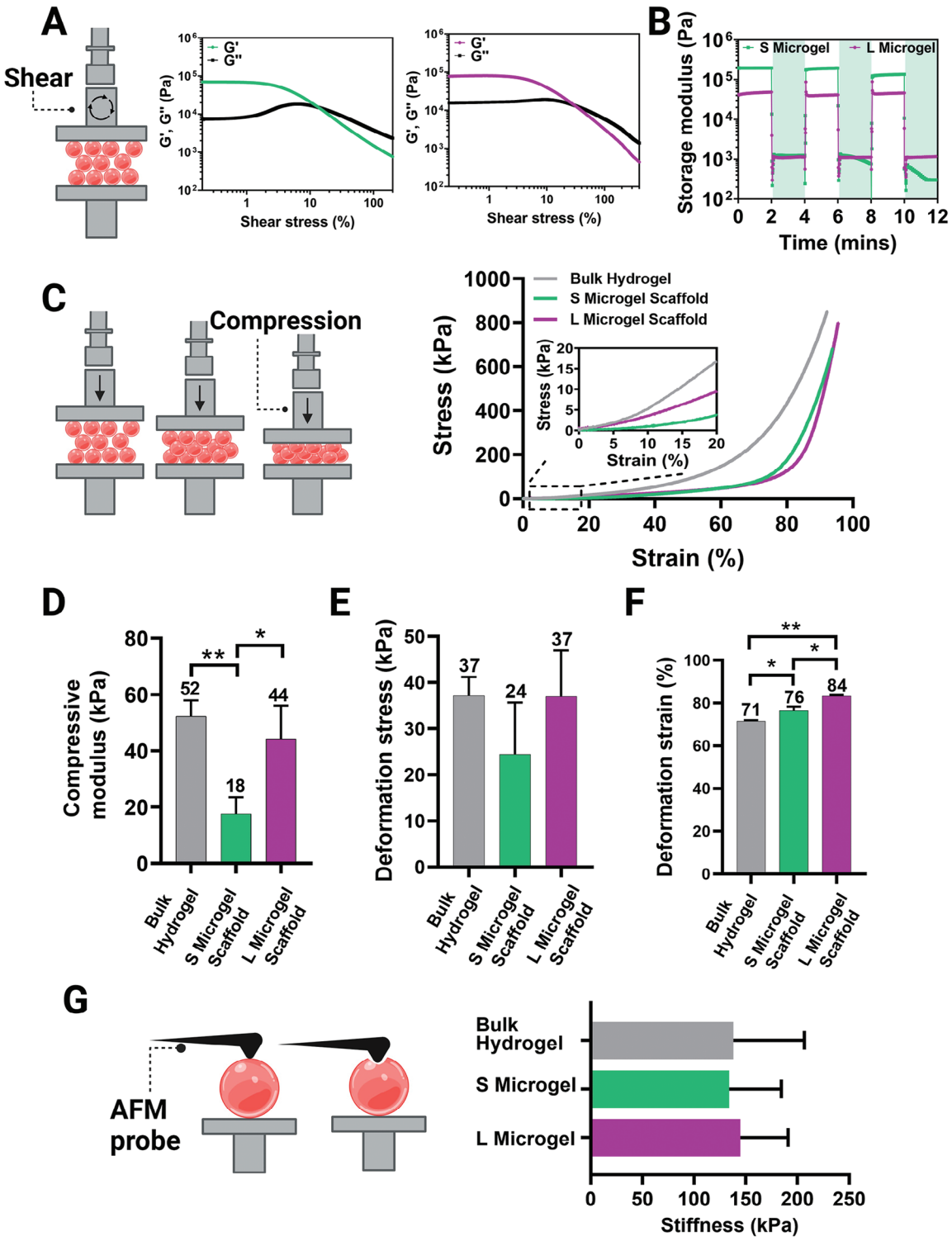

Figure 5. Mechanical properties of bulk hydrogel, small (S) and large (L) microgels, and microgel scaffolds. A) Schematic representation of rheological analyses on silk microgels, data showing the changes in storage and loss modulus over increasing shear stress (%) for Sand L microgels. Strain amplitude sweep tests were performed under oscillatory shear (frequency of 1 Hz) with a log ramp-up rate from 0.2% to 400% shear strain over 8 min. B) Shear-thinning and recovery measurements of S and L microgels performed with an oscillatory 0.2% shear strain for 2 min (1 Hz frequency) followed by a 200% shear strain (1 Hz frequency) for 2 min, repeated over 12 min. C) Schematic representation of compression testing and data showing representative stress-strain curves. D) Compressive moduli of bulk hydrogels and S andL microgel scaffolds. E,F) Deformation stress and deformation strain (%) for bulk hydrogels and microgel scaffolds. G) Schematic representation of AFM-based nanoindentation and stiffness measurements of bulk hydrogels and S and L microgels. Data are mean ± SD, N = 5-11.

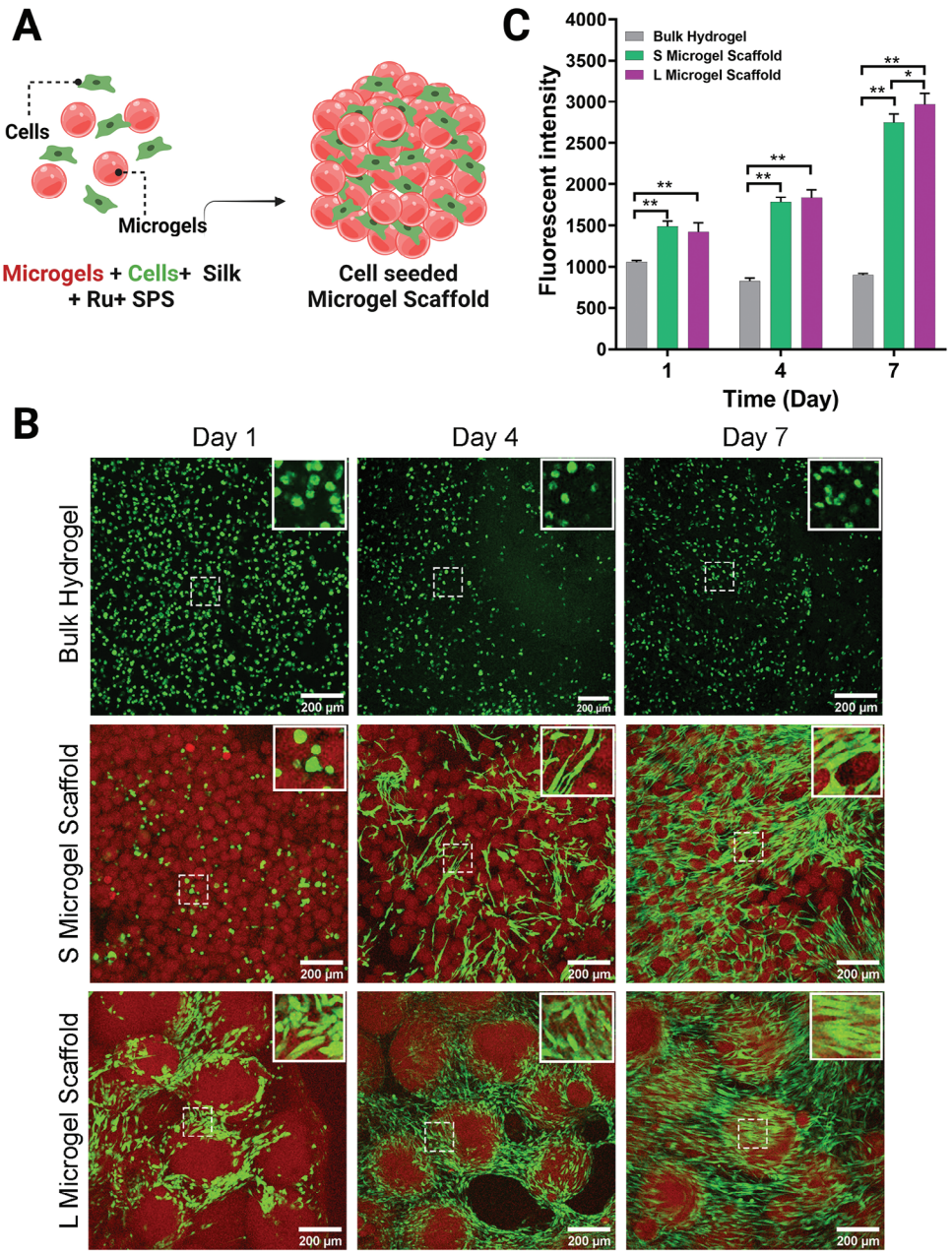

Figure 6. Cell encapsulation and proliferation within the bulk hydrogel and microgel scaffolds. A) Schematic representation of cell encapsulation within the microgel scaffold. B) Confocal images of encapsulated human dermal fibroblast cells within bulk hydrogel and small (S) and large (L) microgel scaffolds at 1, 4, and 7 days. Live cells are stained with Calcein-AM (green) while the microgels are red. Scale bars are 200 µm. C) Proliferation of human dermal fibroblast cells encapsulated within the bulk hydrogel and S and L microgel scaffolds over 7 days measured by the alamarBlue cell proliferation assay. Data are mean ± SD, $N = 6$.

distribution of cells within the hydrogel and in the pores of the microgel scaffolds. The cell morphology and proliferation after 1, 4, and 7 days were observed by staining live cells with Calcein-AM (Figure 6B). At day 1 post-seeding, cells assumed a rounded morphology within the bulk silk hydrogels and small microgel scaffolds but were highly spread on the microgel surface and within the pores of the large microgel scaffolds. This is likely due to the larger diameter (375 µm) and pore size (192 µm) available in the large microgel scaffold which allows for the better spreading of cells compared to the small microgel scaffold (with microgel size of 98 µm and pore size of 29 µm) and bulk hydrogels (with nanopores). No cell spreading and proliferation were observed within the bulk hydrogels over 7 days, likely due to the nano-scale pores and the slow degradation rate of the bulk hydrogel. However, after 4 days, cell spreading was improved within the small microgel scaffolds compared to that on day 1, and cells proliferated within both small and large microgel scaffolds. Interestingly, in the small microgel scaffolds, the cells spread within the pores

or spanned the surface of more than one microgel, with only a small number of cells spreading on the surface of a single microgel. This is likely due to the small size of the microgels and small pore sizes available between them which are in the size range of single-spread cells. In the large microgel scaffolds, on the other hand, multiple cells were typically found on the surface of a single microgel, and networks of cells were spreading within the scaffold pores. This is in line with previous work on cell spreading on hyaluronic acid microgels crosslinked to form microgel scaffolds by PEG, where cells wrapped around large particles and adopted a more spread/flattened shape.[16] After 7 days, cells proliferated within the pores of the microgel scaffolds and covered the surface of the microgels. Cell proliferation was quantified using the alamarBlue cell metabolic assay after 1, 4, and 7 days. As shown in Figure 6C, cell metabolic activity was higher within the small and large microgel scaffolds compared to the bulk hydrogels at each time point ($p < 0.01$). Over the 7-day period, cells proliferated within the small and large microgel scaffolds, but not in the bulk hydrogels. This demonstrates that silk microgel scaffolds can support cell interactions in vitro, including cell encapsulation, adhesion, spreading, and proliferation. Bulk hydrogels on the other hand supported cell encapsulation and survival, but the cells remained largely rounded and did not proliferate over the 7-day period. As the two material types are made using the same crosslinking chemistry, these effects are ascribed to the microporous nature of the microgel scaffolds, where cells are not relying on silk degradation to remodel their microenvironment but where relying on the micron size pores that allow for cell proliferation and material remodeling. Therefore, silk microgel scaffolds provide a compelling material platform for tissue engineering.

2.7. Microgel Scaffolds Support Improved Tissue Infiltration and Material Remodeling In Vivo Relative to Silk Bulk Hydrogels

To test the effect of hydrogel morphology on tissue responses and integration in vivo, silk bulk hydrogels, small and large microgel suspensions (unannealed), and small and large microgel scaffolds (annealed) were implanted in subcutaneous pockets in mice for 4 weeks (**Figure** 7A). All animals survived the surgical procedure and showed no signs of irritation in the implant area over the course of the study. At the 4-week timepoint, samples were adhered to the skin, with bulk hydrogels, microgel scaffolds, and large microgel suspensions easily located for explantation (Figure 7B), while small microgel suspensions were harder to locate as in some animals they appeared to have dispersed over a large surface area relative to other samples. This is one of the key advantages of annealed scaffolds over microgel suspensions when used in tissue regeneration, as annealing provides stabilization in wet or mobile environments, such as with tissue implants or wound grafts.[4]

The silk samples and the surrounding skin were explanted and processed for histological and immunohistochemical analyses, including staining with H&E for overall tissue morphology, Masson's trichrome for collagen deposition and tissue remodeling, and immunostaining for CD68 (macrophages), MHCII and CD206 (broadly M1 and M2 macrophages, respectively). Gross morphological examination showed the mouse skin (Figure 7C) and panniculus carnosus muscle overlaying the implants (Figure 7D–H). The implants occupied a similar volume in the subcutaneous pockets as determined by the cross-sectional implant area (Figure S11, Supporting Information). However, small microgel suspensions were more heterogeneous in their distribution and some samples appeared to have dispersed over a wider area than the bulk and microgel scaffold samples. In fact, in some small microgel suspension samples, the microgels were found in two distinct areas within the subcutaneous pocket with adipose tissue between them, confirming sample dispersion. However, overall microgels remained close to one another with cells and tissue between them even in microgel suspension samples (Figure 7E,F). As expected, the bulk silk hydrogels supported minimal tissue ingrowth over the 4-week period, with most of the sample remaining acellular and surrounded by a collagen-rich fibrous capsule (Figures 7D and 8A). Only minor and inconsistent areas of tissue infiltration into bulk hydrogels were observed and appeared to be due to mechanical damage to the hydrogel during implantation resulting in a conduit for tissue ingrowth, rather than consistent hydrogel degradation (Figure 7D). On the other hand, both small and large silk microgel suspensions supported cell ingrowth and tissue deposition between individual microgels throughout the implants (Figure 7E,F). There were however differences between small and large microgel suspensions, with tighter packing of small microgels allowing less space between individual particles. The overall cellularity within the implant area (**Figure** 8F,G) demonstrated the highest level of cellularity associated with large microgel suspension samples, which was significantly higher than that of bulk hydrogels ($p < 0.05$). While other samples did not show significant differences in the overall cell number associated with the implant, there was an obvious difference in cell distribution, where all cells associated with the bulk hydrogels were in the fibrous capsule on the periphery of the implant, while microgel-based samples supported cell infiltration into the construct (Figure 8F). Both small and large silk microgel scaffolds supported cell infiltration, with cell and tissue observed infiltrating from the periphery toward the sample center (Figure 7G,H). However, the tissue infiltration was not as pronounced and homogenous as that observed in microgel suspensions. While there was collagen deposition surrounding the samples, there was a less obvious multicellular fibrous encapsulation response associated with microgel samples (Figure 8B–E), with small microgel suspensions and large microgel scaffolds having significantly thinner fibrous capsules relative to bulk hydrogels (Figure 8H). All microgel samples, in particular, microgel suspensions had collagen deposition and small capillaries between microgels, demonstrating implant remodeling (Figure 8B–E). While a higher number of blood vessels was observed in microgel samples relative to the bulk hydrogel (Figure 8I), this difference was not statistically significant. However, unlike in bulk hydrogels, where the blood vessels were confined to the fibrous capsule, in the microgel samples, the blood vessels were found in the implant, between microgels. Overall, microgel implants supported blood vessels and tissue infiltration into the implant, supporting collagen deposition between the microgels and implant remodeling, with greater cell and tissue distribution seen in the microgel suspensions relative to microgel scaffolds (Figure 8J). This may be due to the closer packing of annealed microgels or due to the fibrous silk interstitial network. We hypothesize that over longer incubation times,

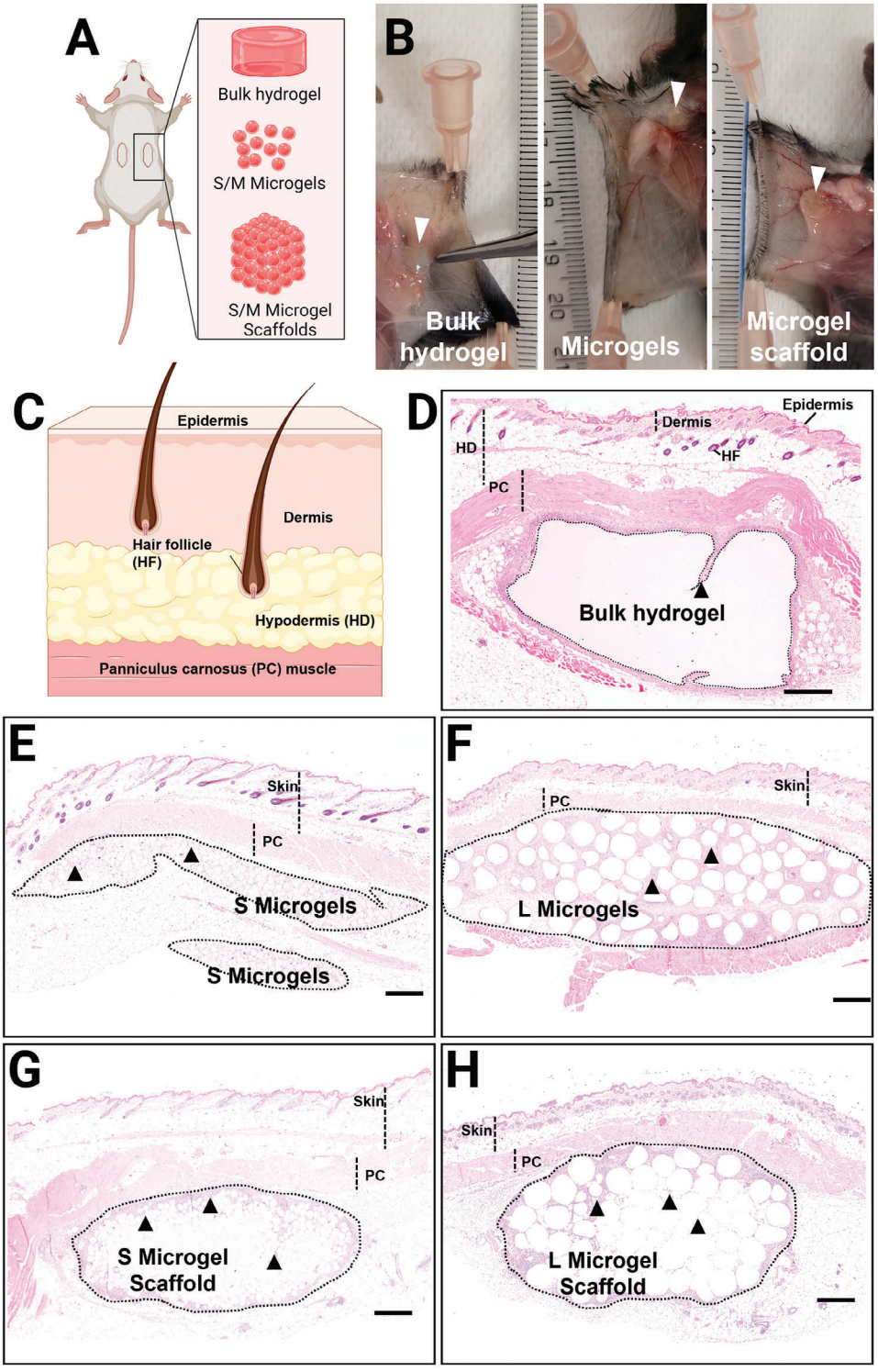

Figure 7. Implantation of silk hydrogels with different morphologies. A) Silk bulk hydrogels, small (S) and large (L) microgel suspensions, and S and L microgel scaffolds were implanted in subcutaneous pockets in mice for 4 weeks. B) Representative images of explants at 4 weeks, showing samples (white arrowheads) adhered to the mouse skin. C) Schematic representation of the mouse skin showing labels relevant to subsequent histological sections. D–H) Representative H&E-stained sample showing gross morphology of silk hydrogel implants, with the dashed outline showing sample boundaries and black arrowheads pointing to cell and tissue infiltration into the sample. D) Bulk hydrogel, E) S Microgels, F) L Microgels, G) S Microgel Scaffold, and H) L Microgel Scaffold. Scale bars are 400 µm.

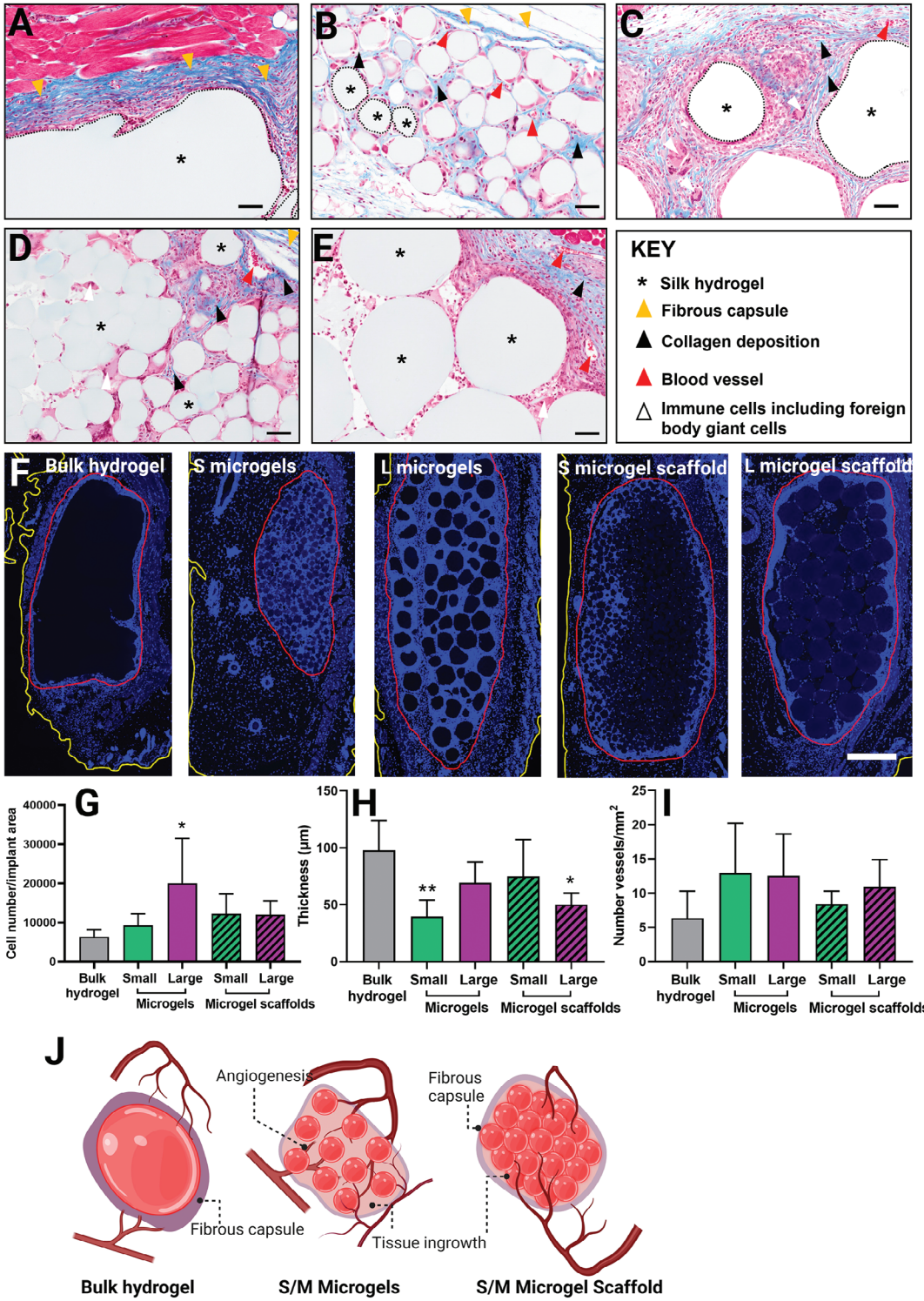

Figure 8. Tissue response to silk hydrogels with different morphologies. Silk bulk hydrogels, small (S) and large (L) microgel suspensions, and S and L microgel scaffolds were implanted in subcutaneous pockets in mice for 4 weeks and stained with Masson's trichrome showing collagen deposition in blue. A) Silk bulk hydrogel, B) S Microgels, C) L Microgels, D) S Microgel Scaffold, E) L Microgel Scaffold. Representative features of the implant, including the fibrous capsule, immune cells, and blood vessels are indicated in the images via arrows as shown in the Key. Scale bars are 50 μm. F) Distribution of cell nuclei in the implants. The red outline shows the implant border and the yellow indicates the tissue border. Scale bar is 500 μm. G) Quantification of the implant area (including fibrous capsule) cellularity. H) Fibrous capsule thickness. I) Implant vascularization. J) Schematic representation of the observations in Figures 7 and 8, showing overall tissue infiltration and vascularization is lowest in bulk hydrogels<Microgel Scaffolds<Microgel suspensions. Data are mean ± SD, $N = 3–5$. Statistically significant differences are relative to bulk hydrogels.

cells would degrade and remodel the silk, depositing more tissue between microgels, with silk degrading completely over time. The degradation rates of di-tyrosine crosslinked materials in vivo are not well characterized in the literature and will be the focus of our future studies. Additionally, as these microgels can be easily loaded with ECM proteins and growth factors, cell and tissue ingrowth, as well as silk degradation, can be further modulated via microgel biofunctionalization.

Immune cells including multinucleated cells were observed in all the samples but were most pronounced in small microgel suspensions (Figures 8 and **9**). As macrophages play a major role in the inflammatory response to biomaterial implants, the macrophage distribution and phenotype in the implant area were studied (**Figure 9**). $CD68^+$ cells (pan-macrophage marker) were found in all the samples, but their distribution and relative amount varied between the different hydrogel morphologies (Figure 9A,B). In bulk hydrogels, $CD68^+$ cells were found in the fibrous capsule surrounding the implant, an unsurprising finding considering the role of macrophages in stimulating collagen deposition and fibrous encapsulation.[49] In microgel suspensions, $CD68^+$ cells were found throughout the sample, but their distribution differed. $CD68^+$ cells were found in proximity to small microgel suspensions, but not completely surrounding them, rather distributed throughout the tissue between individual gels, while in large microgel suspensions, $CD68^+$ cells formed a single layer directly associated with each microgel surface, but less obvious in the tissue between individual microgels (Figure 9A, insets). Analysis of the proportion of CD68+ cells in the implant area showed that bulk hydrogels and large microgel suspensions had the lowest percentage of $CD68^+$ cells, while small microgel suspensions had the highest (Figure 9B). It was interesting to note that while small microgel suspensions had significantly more $CD68^+$ cells than large microgel suspensions ($p < 0.05$), their microgel scaffold counterparts did not show this difference, suggesting that the formation of the scaffolds from the microgels modulated their individual inflammatory response. Samples were also stained for major histocompatibility complex class II (MHCII) (Figure 9C,D) and CD206 (Figure 9E,F) positive cells in the implant area. MHCII is broadly associated with activated M1 macrophages (pro-inflammatory), while CD206 is associated with M2 macrophages (anti-inflammatory) involved in resolving the inflammatory response and tissue healing.[50,51] Interestingly, small microgel suspensions showed the highest percent of $MHCII^+$ cells in the implant area, significantly higher than that of the bulk hydrogels, large microgel suspensions, and microgel scaffolds, all of which had a similar lower response (Figure 9D). The distribution of $MHCII^+$ cells in bulk hydrogels and microgel scaffolds was similar to most cells found surrounding the implant but with some positive cells between microgels in the microgel scaffold samples. However, small and large microgel suspensions showed an interesting difference in the distribution of $MHCII^+$ cells that was opposite to that of $CD68^+$ distribution. $MHCII^+$ cells were found predominantly in a single layer on the implant surface of small microgels, while they were not intimately associated with the microgel surface, but rather distributed in the tissue between the microgels in the case of large microgel suspensions (Figure 9C, insets). It is important to note that not all $MHCII^+$ cells are necessarily macrophages, as dendritic cells,[52] B and activated T cells[53] can express MHCII, but are typically CD68 negative.[54] The role of dendritic cells and of the adaptive immune response to biomaterial implants is much less well understood relative to macrophages and will be the focus of our future investigations in this area. Regardless, the observed differences point to the role of microgel size and format (suspension versus scaffold) is modulating the inflammatory and immune response to implants, allowing greater control over implant design without having to change the biomaterial choice or chemical composition. The advantages of annealed microgel scaffolds over microgel suspensions and bulk hydrogels have been shown with other material types. For example, in one study, PEG-based silk microgel scaffolds promoted a regenerative tissue response in cutaneous wounds, accelerating wound re-epithelialization and promoting regeneration of hair follicles and sebaceous glands (structures not seen in scar tissue) whereas such positive responses were not observed with non-annealed microgels.[9] In another study, the injection of hyaluronic acid-based microgel scaffolds in stroke cavities in mice exhibited a tissue remodeling response by reducing inflammatory response while increasing vascularization compared to the bulk hydrogels.[15] These studies demonstrate the utility of the annealed microgel scaffolds in tissue engineering and regenerative medicine and our current work offers an additional versatile silk-based platform toward these applications.

Finally, bulk hydrogels expressed the highest percent of $CD206^+$ cells (Figure 9F), a result that is not unexpected as these materials were further along the resolution stage of the inflammatory response; however, they also did not support good cell infiltration and tissue remodeling but instead resulted in biomaterial encapsulation, a response not useful to most tissue engineering approaches. The distribution of $CD206^+$ cells in small and large microgel suspensions was like that of $CD68^+$ cells.

The dependence of foreign body immune response on the implant size has been shown for a number of other materials including alginate and poly-(DL-lactide-co-glycolide) (PLGA).[55,56] Implanted alginate microgels at the size of 1.5 mm and above significantly abrogated foreign body reactions and fibrosis compared to the smaller spheres.[55] Poly-(DL-lactide-co-glycolide) (PLGA) microparticles with the small size of 5.8 μm increased cellular and macrophage influx and collagen deposition compared to the large size microparticles of 29.8 μm, demonstrating the suitability of the large microparticles for drug delivery applications.[56] These studies and the current results show the important influence of size and material format on immune response for different applications, and in particular the utility of large microgel suspensions and both small and large microgel scaffolds in tissue engineering and regenerative medicine applications. Future studies will focus on detailed tuning of microgel properties for specific tissue responses, as well as their performance in functional tissue injury models.

3. Conclusion

In this work, we have demonstrated a novel and cytocompatible method to generate silk-based microgels with the ability to load/encapsulate cells during microporous microgel scaffold formation. Two sizes of small and large microgels with a final average diameter of 98 ± 18 and 375 ± 28 μm, respectively, were

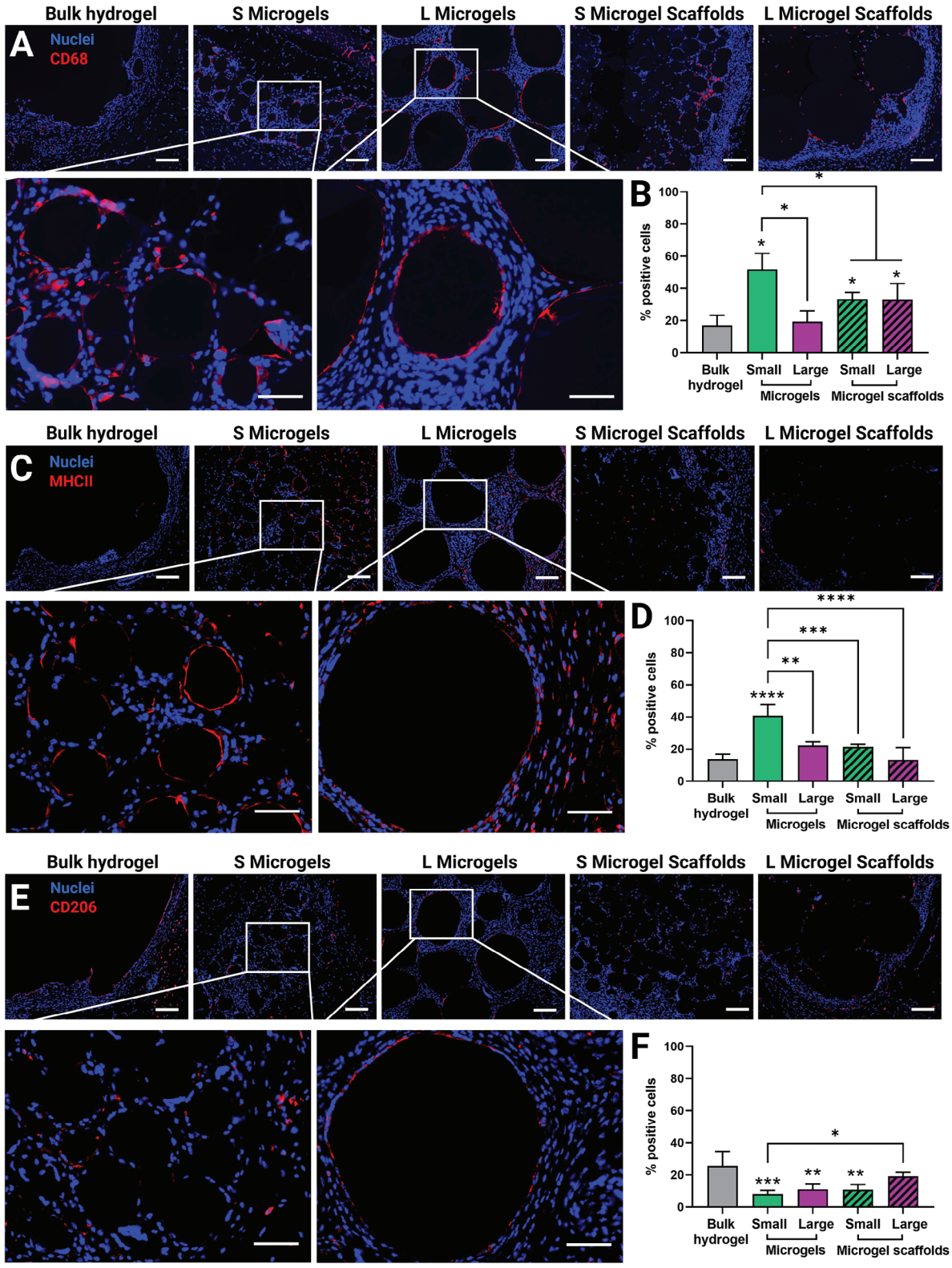

Figure 9. Inflammatory response to silk hydrogels with different morphologies. Silk bulk hydrogels, small (S) and large (L) microgel suspensions, and S) and large L microgel scaffolds were implanted in subcutaneous pockets in mice for 4 weeks and stained with antibodies against CD68, MHCII, CD206 (red), and DAPI nuclear stain (blue). Scale bars are 100 μm in top rows and 50 μm in zoomed-in images. A) Expression of CD68, B) percent of CD68 positive cells, C) expression of MHCII, D) percent of MHCII positive cells, E) expression of CD206, F) Percent of CD206 positive cells in the implant area. Data are mean ± SD, $N = 3–5$. Statistically significant differences are relative to the bulk hydrogel unless indicated otherwise.

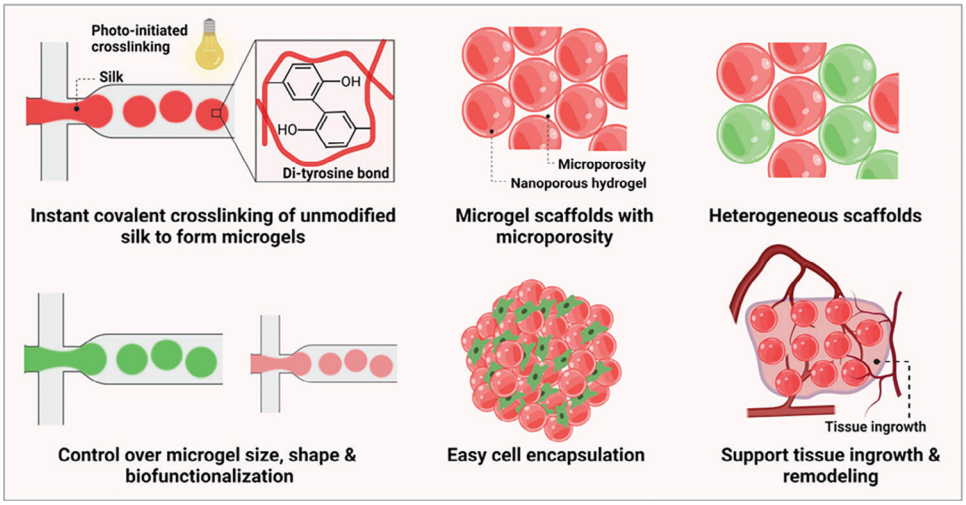

Figure 10. Summary of the advantages of the photocrosslinked silk microgels and microgel scaffolds developed in this work.

generated by flow-focusing microfluidic devices and were stabilized via visible light-initiated crosslinking of native tyrosine residues in silk. Small or large silk microgels were annealed to one another using silk as a glue via visible light-initiated di-tyrosine crosslinking to form small and large silk microgel scaffolds. Investigation of the mechanical properties showed that the compressive modulus of microporous microgel scaffolds can be modulated by varying the size of microgels and demonstrated that the microgel scaffolds are easily handled and resist deformation. More importantly, we demonstrated that the system used in this study enables in situ encapsulation of cells within the micropores of silk microgel scaffolds during the formation of the microporous scaffold from individual microgels. We showed that the silk without any modification/biofunctionalization can be used as glue to anneal microgels to one another in the presence of cells using a cytocompatible visible-light di-tyrosine crosslinking method. In vivo studies also showed that the microporous silk microgel scaffolds supported improved cell and tissue ingrowth and remodeling compared to the bulk silk hydrogels, and microgel size and material format modulated the inflammatory response to these implants. Overall, this work demonstrates a novel microgel system with tunable matrix properties and porosity which foster enhanced cell growth and infiltration both in vitro and in vivo (**Figure 10**). In the future, using microgel scaffolds with different microgel sizes provides an avenue to tune both spatial and temporal control over molecule release profiles, scaffold mechanics, porosity, and degradation profiles. This provides scope for both fundamental studies of cellular-matrix interactions as well as for advanced and highly tuned transplantable scaffolds and injectable biomaterials for regenerative medicine.

4. Experimental Section

Preparation of the Silk Solution: Silk fibroin solution was prepared as previously described.[44,46] Briefly, *bombyx mori* silk cocoons (Sato Yama, Japan) were cut into small pieces and boiled in 0.02 M sodium carbonate solution (2.5 g L^{-1}) for 30 min to remove sericin. After washing under running water, the fibers were dried at room temperature. The dried silk fibroin fibers (0.25 g mL^{-1}) were dissolved in lithium bromide (9.3 M) at 60 °C for 4 h. The dissolved silk solution was dialyzed against water (SnakeSkin, 3500 MWCO, Thermo Fisher Scientific) for 3 days (changed two times per day) and centrifuged three times at 8900 rpm (Allegra X-30R) for 20 min at 4 °C. The silk solution concentration was determined as 6–9% w/v after drying a known amount of silk solution and weighing the dried remaining film. The silk solution was stored at 4 °C.

Design and Fabrication of Microfluidic Devices: The channel pattern of flow-focus microfluidic devices was drawn using computer-aided design software (OnShape). The designed patterns were etched onto the surface of acrylic sheets (4.4 mm thickness) using a CO_2 laser cutter (Trotec SP500) and cut to the size of a standard glass cover slip (27 × 77 mm). Two different sizes of channels were generated to produce small and large microgels (Figure S1, Supporting Information). The channel features were verified using an optical microscope. To produce the final microfluidic devices, multiple molding processes were used. The detailed description and the schematic fabrication process of the microfluidic devices are presented in Figure S2 (Supporting Information). The STL files for all designs in this study are available in the Supporting Information.

Formation of Silk Microgels and Bulk Hydrogels: The spherical silk microgels were formed using a flow-focusing microfluidic device with two inlets and one outlet (Figures S1–S3, Supporting Information). One inlet was reserved for the heavy mineral oil (SKYDD, IKEA) plus 6% w/w span-80 (Sigma), and the other inlet was used for the silk solution plus the visible-light initiating compounds of tris(2,2′-bipyridyl)dichlororuthenium(II) hexahydrate (Ru) and sodium persulfate (SPS). The silk solution was freshly prepared from the concentrated isolated silk solution (6–8%) at a total concentration of 3% w/v in deionized water and mixed with Ru and SPS to a final concentration of 0.08 and 0.8 mM, respectively. Heavy mineral oil containing span-80 and silk solution containing Ru and SPS was loaded in plastic syringes and the air bubbles were removed completely from the syringes. Two syringe pumps (Nexus 6000 and New Era NE-4002X) were used to separately control the flow rates of the oil and the silk solution. The flow rate of 400 µL h^{-1} for oil and the flow rates of 100 and 600 µL h^{-1} were used for silk solution to produce small and large microgels, respectively. The silicon tubing used for the inlet of silk solution, the outlet, and the syringe containing the silk solution plus Ru and SPS were covered with foil to prevent light exposure. In addition, the microfluidic device was protected from light during the experiment to prevent the gelation of the silk solution inside the channels before microgel formation. The microgels were collected in a centrifuge tube covered with foil. After the microgels were collected, they were exposed to 30 mW cm^{-2} light with a distance of 5–8 cm and at 400–450 nm for 20 min with a regular rotation of the centrifuge tube to ensure all

microgels were exposed to light. The crosslinked microgels were centrifuged at 1000 rpm (Eppendorf 5810R) for 3 min to remove the oil and washed in PBS (PBS without Ca^{2+} and Mg^{2+}, pH 7.4, Medicago) followed by centrifugation at 4000 rpm for 5 min. The supernatant was aspirated, and the above procedure was repeated until all the oil and surfactant were removed (≈5–6 times). The microgels were kept in PBS at 4 °C and used within 1 month.

For the encapsulation of fluorescently tagged bovine serum albumin (BSA) in the microgels, BSA-Alexa Fluor 594 conjugate (Invitrogen, ThermoFisher Scientific) and BSA-Alexa Fluor 488 conjugate at a total concentration of 0.1 mg mL^{-1} were added to the silk solution. To prepare BSA-Alexa Fluor 488 conjugate, 12 µL of Alexa Fluor-NHS (Alexa Fluor 488-SDP ester, stocking solution 10 mg mL^{-1} in DMSO) were added to 2 mL of BSA (2 mg mL^{-1}) and kept at RT for 30 min–1 h to mix. Then the mixture passed through the column for purification.

For the silk bulk hydrogel production, the silk solution plus Ru and SPS (50 µL, 3%) was added to a silicon mold (Figure S7C, Supporting Information) made by a double molding process (Figure S7, Supporting Information) and exposed to 30 mW cm^{-2} light with a distance of 5–8 cm and at 400–450 nm for 5 min. The hydrogels were then removed from the mold and stored in PBS at 4 °C. The STL file of the design is available in the Supporting Information.

Generation of Silk Scaffold from Microgel Building Blocks: To generate silk microgel scaffolds from the microgel building blocks with similar volume sizes, the microgels (≈50–100 µL) were pipetted into the mold prepared from 1 mL plastic syringe (Terumo, 4.73 mm inner diameter) (Figure 2B). The mold was then placed inside a 1 mL microcentrifuge tube and centrifuged at 4000 rpm for 3 min. The PBS supernatant was aspirated and 40 µL of 3% (w/v) silk solution containing Ru and SPS (silk precursor solution as described in 'Formation of Silk Microgels and Bulk Hydrogels' above) was added to the microgel and mixed well with the pipette tip and then centrifuged at 4000 rpm for 5 min. The supernatant silk solution containing Ru and SPS was aspirated from the top of microgels and the microgels were exposed to 30 mW cm^{-2} light at 400–450 nm for 5 min to form crosslinked microgel scaffolds. The scaffold was removed from the syringe mold by pushing the plunger slowly up and then separating the scaffold from the bottom of the plunger. The scaffolds were then transferred to PBS and stored at 4 °C until further use.

Measurements of Microgel Size and Microgel Scaffold Pore Size and Void Fraction: To measure the size/diameter of microgels, they were imaged in oil and PBS using an Olympus microscope system (IX83, Olympus Corporation, Shinjuku) after crosslinking. After imaging the microgels, the diameter of the microgels was measured using ImageJ (NIH) ($n = 60$–100). The swelling ratio of single microgels was determined as (r^3_{PBS}/r^3_{oil}), where r is the radius of the microgel. To obtain fluorescent images of microgels, the microgels (100 µL) were placed overnight in rhodamine solution (200 µL, 50 µg mL^{-1}, ThermoFisher Scientific) at room temperature to adsorb the fluorescent rhodamine onto the silk microgels. The microgels were then washed 3–4 times by centrifugation in PBS before confocal imaging (laser scanning microscope, Leica Confocal microscope, TCS SP2).[9,17]

Microgel scaffolds ($n = 4$–5) were made using the silk microgels (microgels labeled with rhodamine, described above). Using the confocal microscope, z-slices of 12 µm were taken in each gel, spanning a total distance of 150–250 µm. The images were analyzed for individual pore areas using ImageJ software (NIH) ($n = 70$–140). To obtain the pore diameter, the pore areas were treated mathematically as circles, and the diameter of these circles was calculated.[17] To show the porosity of silk microgel scaffolds, the microgel scaffolds were immersed in a solution of Fluorescein isothiocyanate-dextran (150 KDa, 200 µL, 0.2 mg mL^{-1}, Sigma) for 2 h at room temperature to fill the unoccupied volume of the scaffolds.[18] The microgel scaffolds were then washed with PBS three times (5 min each) and then imaged with a confocal microscope. The images were analyzed for 2D average void space fraction by $(A_{void})/(A_{total})\times100$, where A_{void} is the total void area and A_{total} is the total area.[16]

Scanning Electron Microscopy (SEM): The microgel scaffolds and bulk hydrogels ($n = 3$–4) were sequentially dehydrated in ethanol (30, 50, 70, 90, 100 v/v%) using a microwave processor (BioWavePro+, Pelco). Dehydrated samples were subsequently dried using critical point drying (Autosamdri-815, Tousimis), mounted onto double-sided carbon tape, lined with silver glue, and coated with platinum (K575X, EMITECH). Samples were imaged using a Hitachi SEM3400 electron microscope under a high vacuum using a beam power of 15 kV and probe current of 30 µA.

Mechanical Properties of Microgel Scaffolds and Bulk Hydrogels: The compressive mechanical properties of the microgel scaffolds and bulk hydrogels ($n = 4$–5) were measured using an Instron 5543 mechanical tester equipped with a 50 N load cell at a compression rate of 1 mm min^{-1} in a PBS bath set to 37 °C. The scaffolds and hydrogels (4.1–4.7 mm diameter and 1.1–2.8 mm height) were compressed until reaching 0.1 mm their height. The Young's modulus was extracted from the slope of the linear region of the stress–strain curve ranging from 0% to 40% strain. The yield stress and strain were extracted from the x-y coordinates of the corner frequency of the initial linear region (0–40% strain) and exponential rise (80–95% strain).

Atomic Force Microscopy (AFM): All data were acquired with the JPK NanoWizard4 Bio-AFM with a spherical probe (2 µm spherical diameter Borosilicate unmodified probe, Novascan, spring constant 0.35 N m^{-1}). Bulk hydrogels and both small and large microgels were dispersed onto fluorodishes (Coherent, FD35) and submerged in PBS at 37 °C throughout the measurements. The tip spring constant was calibrated on glass in PBS at 37 °C prior to the experiment. Using contact-force microscopy mode, 20–25 force curves (5 µm at 2 µm s^{-1}) were taken at over ten 8 × 8 µm regions/particles per size. The curves were loaded in the JPK Data Processing software to calculate the elastic modulus. An average of 200 curves was used for the final modulus value. The following analysis steps were performed: 1) Gaussian smoothing of the curve with a smoothing width of 3.00; 2) Baseline subtraction with tilt using the last 50% of the curve along the x-axis; 3) Automatic contact point adjustment; 4) Vertical tip position calibration using the smoothed height; 5) An elasticity fit using the Hertz/Sneddon model with a spherical tip shape with a 1 µm tip radius and 0.50 Poisson ratio. At least 8 particles were used per size group, with over 20 force curves taken per microgel, and care was taken to measure force curves within the central 1/3 of microgels to avoid edge effects.

Rheology: For rheology experiments, the silk microgels were centrifuged at 4000 rpm for 5 min, PBS aspirated, 3% silk solution containing Ru and SPS was added, and the mixture was centrifuged at 4000 rpm for 5 min. The excess solution was aspirated and the microgels were transferred to the plate of the rheometer by spatula. The rheological measurements were taken with an Anton Parr MCR 302 Rheometer using a parallel plate geometry (25 mm diameter, 0.8 mm measuring distance). Shear rate sweeps were performed with a log ramp from 0.01 to 10 1 s^{-1} shear rate over 6 min. Strain amplitude sweep tests were performed under oscillatory shear (frequency of 1 Hz) with a log ramp-up rate from 0.2% to 400% shear strain over 8 min. Shear thinning and recovery (self-healing curve) measurements were performed with an oscillatory 0.2% shear strain for 2 min (1 Hz frequency) followed by a 200% shear strain (1 Hz frequency). This was repeated two times more in a row.

Swelling and Degradation of Bulk Hydrogel and Microgel Scaffolds: To measure the swelling ratio, the excess water on the gel surface was removed gently. The hydrated microgel scaffolds and bulk hydrogels ($n = 5$) were weighted. Samples were then dried overnight at 60 °C and weighed. The swelling ratio was determined as W_h/W_d, where W_h is the mass of the hydrated and W_d is the mass of dry microgel scaffold or bulk hydrogel.[33]

To measure the relative degradation rate, the microgel scaffolds and bulk hydrogel ($n = 5$) were weighed and then incubated in protease from streptomyces griseus (protease XIV, 2U mL^{-1} in PBS, 1 mL, Sigma) or PBS at 37 °C (1 mL) for 2 days. The protease solution or PBS was removed at each time point and the microgel scaffold and bulk hydrogel were washed with water (3 times) and dried at 60 °C. The dried microgel scaffolds and bulk hydrogel were weighed and placed in the fresh protease or PBS solution and the whole process was repeated every 2 days and up to 8 days. The percentage of remaining mass over time was calculated as $100 - ((W_0 - W_t)/W_0 \times 100)$, where W_0 is the weight of dried microgel scaffold or bulk hydrogel at time 0 and W_t is the dry weight after time t.[33]

In Vitro Cell Adhesion and Proliferation Studies—Cell Maintenance: The primary human dermal fibroblast cells were cultured according to

standard procedure. Briefly, Dulbecco's Modified Eagle Medium (DMEM, high glucose, Sigma) was supplemented with 10% Fetal Bovine Serum (FBS, Bovogen Biologicals), and 1% penicillin-Streptomycin (Sigma). Cells were passaged every 3–4 days using trypsin-EDTA solution (1X, Sigma) at subconfluence and incubated at 37 °C, 5% CO_2, and 90% humidity. Cell passages 2–7 were used for cell experiments.[57]

In Vitro Cell Adhesion and Proliferation Studies—Cell Culture and Proliferation: Before encapsulating cells, the cells were centrifuged and washed with PBS (3 times). Then, ≈80 µL of sterilized microgels (under UV for 1 h) were transferred to the plastic syringe mold ($n = 4$, prepared as described in 'Generation of Silk Scaffold from Microgel Building Blocks', Figure 2B), centrifuged at 4000 rpm for 3 min and PBS supernatant was discarded. A 50 µL of cells from a stock solution of 2×10^6 cells mL^{-1} was transferred to the mold containing microgels and mixed with a pipette tip, centrifuged at 4000 rpm for 3 min. The supernatant was aspirated and then a 40 µL of silk solution containing Ru and SPS (3% (w/v), sterilized by passing through 0.22 µm filter) was added and mixed well with microgels and cells and centrifuged again at 4000 rpm for 5 min. The supernatant was discarded, and the scaffold was exposed to 30 mW cm^{-2} light of 400–450 nm for 5 min to form encapsulated cells within a crosslinked microgel scaffold. To form encapsulated cells in the bulk hydrogels ($n = 4$), 5 µL of a stock solution of 20×10^6 cell mL^{-1} was mixed with the silk solution containing Ru and SPS (3%) inside the silicon rubber mold 2 (Figure S6, Supporting Information) and exposed to 30 mW cm^{-2} light of 400–450 nm for 5 min to form encapsulated cells within bulk hydrogels. The microgel scaffolds and bulk hydrogels encapsulating cells were then transferred to a 48 well-plate containing DMEM and incubated at 37 °C for 1, 4, and 7 days. Importantly, to prevent cell attachment to the well-plate, 200 µL of agarose (10 mg mL^{-1}, Sigma) in PBS (boiled in a water bath for 10 min and sterilized by filtering) was added to each well to coat the bottom and allowed to cool to room temperature before transferring the scaffolds and hydrogel to the well-plate.[16] After 1, 4, and 7 days, each scaffold was washed with PBS (3 times, 5 min each) and then 500 µL of Calcein-AM solution (2 µg mL^{-1}, Invitrogen, ThermoFisher Scientific) was added to the microgel scaffolds and bulk hydrogels and incubated for 15 min at 37 °C. Then, the microgel scaffolds and hydrogels were washed with PBS (3 times, 5 min each) and the live image of cells in microgels was taken by a confocal laser scanning microscope (Leica Confocal microscope) and the images were analyzed using ImageJ software (NIH). Please note that microgels were not stained with any fluorescent molecule and the red color is from the excitation/emission of Ru light initiator remaining in the microgels.

For proliferation evaluation of cells encapsulated within microgel scaffolds and bulk hydrogels ($n = 4$), the alamarBlue assay (Invitrogen, Thermo Fisher Scientific) was used. After 1, 4, and 7 days, 500 µL of alamrBlue in DMEM solution (1:10 ratio) were added to each well and incubated for 4 h at 37 °C. The fluorescent intensity of the solution was then read at 540/600 nm excitation/emission. The alamarBlue in DMEM solution and the scaffolds without cells were used as controls. Experiments were repeated at least three times.[44]

In Vivo Subcutaneous Model: The bulk hydrogel, small and large microgel suspensions, and small and large microgel scaffolds were prepared as described above ('Formation of Silk Microgels and Bulk Hydrogels' and 'Generation of Silk Scaffold from Microgel Building Blocks') and sterilized under UV for 1 h before implantation. All procedures were conducted in accordance with animal ethics protocols approved by the UNSW animal ethics committee (ACEC 21/14B) on 10-week-old female C57/BL6 mice. Mice were placed under general anesthesia of isoflurane (1 L min^{-1} oxygen, 3–4% induction, 2–3% maintenance). The back of each mouse was shaved, and the surgical site was disinfected with betadine and isopropanol wipes thrice each, followed by a subcutaneous administration of buprenorphine at 0.1 mg kg^{-1}. A single surgical incision was made below the neck and subcutaneous pockets were created toward the left and right hind legs using blunt forceps. The bulk hydrogel, small and large microgel suspensions, and small and large microgel scaffolds were implanted. One randomized sample was implanted in each subcutaneous pocket ($n = 5$). The incision was closed with surgical clips, Vetbond tissue adhesive (3 M) was applied on the wound site, and anti-bacterial wound spray (Cetrigen) was applied around the wound site. Surgical clips were removed on day 10 post-surgery. Post-operatively, animals were housed with unlimited access to food and water.

Histological and Immunohistochemical Analysis of Implants: At 4 weeks post-surgery, animals were euthanized using carbon dioxide (1.6 mL min^{-1}), followed by secondary euthanasia by cervical dislocation. The implanted site with bulk hydrogels, small and large microgel suspensions, and small and large microgel scaffolds and the surrounding tissue were explanted for histological analyses. Explants were fixed in 10% neutral buffered formalin for 48 h at 4 °C, transferred to 70% ethanol for 24 h at 4 °C, and embedded in paraffin wax. Whole tissue samples were embedded such that sectioning was conducted perpendicular to the implanted scaffolds. Paraffin-embedded samples were sectioned to a thickness of 5 µm and collected on SuperfrostTM Plus microscope slides (ThermoFisher). Sections were deparaffined by two 5 min incubations of xylene and then rehydrated into deionized water via a descending gradient of ethanol incubations (100% twice, 90%, 70% then water for 5 min each). Samples were then stained by hematoxylin and eosin (H&E), Masson's Trichrome, or processed for immunohistochemical analyses.

For H&E staining, rehydrated samples were stained in Gill's no.3 hematoxylin (Vector Laboratories) for 5 min, rinsed in 1% acid alcohol (1% hydrochloric acid in 70% ethanol), and incubated in bluing solution (0.1% sodium bicarbonate in distilled water) for 60 s, with deionized water rinses done between each step. Slides were stained with alcoholic eosin for 5 min then dehydrated using an ascending gradient of ethanol (90%, 100% twice for 1 min each), cleared with two incubations of xylene for 5 min each, and mounted.

For Masson's Trichrome staining, staining was performed using a kit applied according to the manufacturer's instructions. Briefly, samples were mordanted in preheated Bouin's solution for 15 min at 56 °C and washed in tap water. Samples were then stained sequentially with Gill's no.3 hematoxylin, Biebrich scarlet-acid fuchsin, phosphotungstic/phosphomolybdic acid solution, and aniline blue solution for 5 min each with deionized water rinses in between each stain. Samples were differentiated in 1% acetic acid for 1 min before dehydration with an ascending gradient of ethanol, cleared with xylene, and mounted as previously described above. All slides were imaged using an Aperio Scanscope XT scanner (Leica) with a 40x objective and viewed using ImageScope software (Leica).

For immunohistochemical analyses, sections were deparaffined by two 5 min incubations in xylene and then rehydrated into deionized water via a descending gradient of ethanol incubations (100% twice, 90%, 70% then water for 5 min each). Antigen retrieval was performed using a decloaking chamber (citrate buffer at 110 °C for 5 min and rinsed in water 3 times).

Slides were then incubated in 0.1 M glycine for 30 min followed by one rinse in TBS 1X. All the slides were blocked with 10% donkey serum for 60 min at room temperature. Primary antibody cocktails (CD68 (Abcam, ab125212, 1:500), CD206 (Abcam, ab64693, 1:250), MHCII (Abcam, ab180779, 1:100)) were added and incubated for 60 min at room temperature followed by two rinses with TBS 1X. The secondary antibody, Alexa Fluor 594 (ab150064, 1:500) was added and incubated for 30 min followed by 2 washes in TBS 1X. Cell nuclei were counterstained with spectral DAPI for 5 min followed by one wash. Slides were cover-slipped following the addition of ProLong Gold Antifade Mountant (Thermo Fisher Scientific) and all stained histology sections were scanned using an Olympus VS200 slide scanner.

Images were analyzed and processed using analysis packages built into the open-access software QuPath[58] and using Image J.[59] To quantify the implant area, an annotation (or region of interest [ROI]) was overlayed to the scaffold area with an extra distance of 100 µm to the edge of the implant. At these distances, the scaffold as well as the fibrous capsule was covered. To quantify the cellularity, the cell detection command (based on a number of DAPI-positive cells) built into QuPath was run to quantify cell numbers within the allocated ROI. Fibrous capsule thickness was measured in three regions of the implant (top, bottom, middle), on the skin side. A grid was overlayed over each region and three measurements were made where the grid intersected with the fibrous capsule. Implant vascularization was quantified by counting the number of blood vessels (clear lumen area, filled with red blood cells) in H&E stained samples and

normalized to the implant area. QuPath software was trained to automatically detect and count M1, M2, and pan macrophages across the whole section. To perform automated detection of macrophages, an object classifier that allowed identification of specific cell types within the image based on initial user identification and classification was first trained. This classifier was then applied to all the sections for each antibody to detect the percentage of positive cells per marker and per ROI.

Statistical Analysis: Data were presented as mean ± standard deviation (SD). Statistically significant differences were determined by one- or two-way analysis of variance (ANOVA) and the Tukey post-test or by student's *t*-test. Statistical significance was reported at $p < 0.05$ and indicated in the figures as $^{*}p < 0.05$, $^{**}p < 0.01$, $^{***}p < 0.001$, and $^{****}p < 0.0001$.

Supporting Information

Supporting Information is available from the Wiley Online Library or from the author.

Acknowledgements

F.K. would like to acknowledge the Vice Chancellor's Fellowship and funding support from the University of New South Wales (UNSW Sydney) to perform this study. J.R.-K. would like to acknowledge funding support from the Australian Research Council (FT210100668), NSW Health Cardiovascular Research Capacity Program Early-Mid Career Researcher Grants, and UNSW Scientia Program. F.Z., K.L., M.M., H.J., and T.M. were supported by the Australian Government Research Training Program Scholarship. The authors acknowledge Naomi Craig for their assistance in animal study. The authors thank Dr Isabel Morrow for their technical assistance and use of facilities at the Electron Microscope Unit (EMU). Histological analyses were carried out using instruments situated in, and maintained by, the Katharina Gaus Light Microscopy Facility with technical assistance from Ms Fei Shang. Katharina Gaus Light Microscopy Facility and EMU are part of the Mark Wainwright Analytical Center at the UNSW Sydney which is in part funded by the Research Infrastructure program at the UNSW. The authors also acknowledge James Tawadros in Makerspace for assistance in laser cutting. The schematic drawings were made using Biorender.

Open access publishing facilitated by University of New South Wales, as part of the Wiley - University of New South Wales agreement via the Council of Australian University Librarians.

Conflict of Interest

The authors declare no conflict of interest.

Data Availability Statement

The data that support the findings of this study are available from the corresponding author upon reasonable request.

Keywords

biomaterials, microgels, porous scaffolds, silk, tissue regeneration

Received: December 4, 2023
Revised: January 7, 2024
Published online:

[1] J. Li, D. J. Mooney, *Nat. Rev. Mater.* **2016**, *1*, 16071.
[2] S. Van Vlierberghe, P. Dubruel, E. Schacht, *Biomacromolecules* **2011**, *12*, 1387.
[3] J. Bae, J. Park, S. Kim, H. Cho, H. J. Kim, S. Park, D.-S. Shin, *J. Indus. Eng. Chem.* **2020**, *89*, 1.
[4] A. C. Daly, L. Riley, T. Segura, J. A. Burdick, *Nat. Rev. Mater.* **2020**, *5*, 20.
[5] K. J. De France, F. Xu, T. Hoare, *Adv. Healthcare Mater.* **2018**, *7*, 1700927.
[6] N. Annabi, J. W. Nichol, X. Zhong, C. Ji, S. Koshy, A. Khademhosseini, F. Dehghani, *Tissue Eng. Part B, Rev.* **2010**, *16*, 0639
[7] J. Alijotas-Reig, M. T. Fernández-Figueras, L. Puig, *Clin. Rev. Allergy Immunol.* **2013**, *45*, 97.
[8] M. P. Lutolf, J. L. Lauer-Fields, H. G. Schmoekel, A. T. Metters, F. E. Weber, G. B. Fields, J. A. Hubbell, *Proc. Natl. Acad. Sci. U. S. A.* **2003**, *100*, 5413.
[9] D. R. Griffin, W. M. Weaver, P. O. Scumpia, D. Di Carlo, T. Segura, *Nat. Mater.* **2015**, *14*, 737.
[10] A. S. Caldwell, B. A. Aguado, K. S. Anseth, *Adv. Funct. Mater.* **2020**, *30*, 1907670.
[11] A. E. Widener, M. Bhatta, T. E. Angelini, E. A. Phelps, *Biomater. Sci.* **2021**, *9*, 2480.
[12] A. S. Caldwell, G. T. Campbell, K. M. Shekiro, K. S. Anseth, *Adv. Healthcare Mater.* **2017**, *6*, 1700254.
[13] N. J. Darling, W. Xi, E. Sideris, A. R. Anderson, C. Pong, S. T. Carmichael, T. Segura, *Adv. Healthcare Mater.* **2020**, *9*, 1901391.
[14] J. E. Mealy, J. J. Chung, H. H. Jeong, D. Issadore, D. Lee, P. Atluri, J. A. Burdick, *Adv. Mater.* **2018**, *30*, 1705912.
[15] L. R. Nih, E. Sideris, S. T. Carmichael, T. Segura, *Adv. Mater.* **2017**, *29*, 1606471.
[16] N. F. Truong, E. Kurt, N. Tahmizyan, S. C. Lesher-Pérez, M. Chen, N. J. Darling, W. Xi, T. Segura, *Acta Biomater.* **2019**, *94*, 160.
[17] E. Sideris, D. R. Griffin, Y. Ding, S. Li, W. M. Weaver, D. Di Carlo, T. Hsiai, T. Segura, *ACS Biomater. Sci. Eng.* **2016**, *2*, 2034.
[18] R. S. Hsu, P. Y. Chen, J. H. Fang, Y. Y. Chen, C. W. Chang, Y. J. Lu, S. H. Hu, *Adv. Sci.* **2019**, *6*, 1900520.
[19] F. Li, V. X. Truong, P. Fisch, C. Levinson, V. Glattauer, M. Zenobi-Wong, H. Thissen, J. S. Forsythe, J. E. Frith, *Acta Biomater.* **2018**, *77*, 48.
[20] F. Li, V. X. Truong, H. Thissen, J. E. Frith, J. S. Forsythe, *ACS Appl. Mater. Interfaces* **2017**, *9*, 8589.
[21] N. J. Darling, E. Sideris, N. Hamada, S. T. Carmichael, T. Segura, *Adv. Sci.* **2018**, *5*, 1801046.
[22] J. Fang, J. Koh, Q. Fang, H. Qiu, M. M. Archang, M. M. Hasani-Sadrabadi, H. Miwa, X. Zhong, R. Sievers, D. W. Gao, *Adv. Funct. Mater.* **2020**, *30*, 2004307.
[23] A. R. Murphy, D. L. Kaplan, *J. Mater. Chem.* **2009**, *19*, 6443.
[24] C. Vepari, D. L. Kaplan, *Prog. Polym. Sci.* **2007**, *32*, 991.
[25] H. Zheng, B. Zuo, *J. Mater. Chem. B* **2021**, *9*, 1238.
[26] H. A. Tran, T. T. Hoang, A. Maraldo, T. N. Do, D. L. Kaplan, K. S. Lim, J. Rnjak-Kovacina, *Mater. Today* **2023**, *65*, 244.
[27] T. K. Mwangi, R. D. Bowles, D. M. Tainter, R. D. Bell, D. L. Kaplan, L. A. Setton, *Int. J. Pharm.* **2015**, *485*, 7.
[28] X. Zhao, Z. Chen, Y. Liu, Q. Huang, H. Zhang, W. Ji, J. Ren, J. Li, Y. Zhao, *Adv. Healthcare Mater.* **2018**, *7*, 1801005.
[29] A. Nisal, R. Sayyad, P. Dhavale, B. Khude, R. Deshpande, V. Mapare, S. Shukla, P. Venugopalan, *Sci. Rep.* **2018**, *8*, 7235.
[30] J. Qu, L. Wang, L. Niu, J. Lin, Q. Huang, X. Jiang, M. Li, *Materials* **2018**, *11*, 1280.
[31] D. Yao, M. Li, T. Wang, F. Sun, C. Su, T. Shi, *ACS Biomater. Sci. Eng.* **2021**, *7*, 636.
[32] K. Numata, P. Cebe, D. L. Kaplan, *Biomaterials* **2010**, *31*, 2926.

[33] M. Baptista, H. Joukhdar, C. R. Alcala-Orozco, K. Lau, S. Jiang, X. Cui, S. He, F. Tang, C. Heu, T. B. Woodfield, *Biomater. Sci.* **2020**, *8*, 7093.
[34] X. Cui, B. G. Soliman, C. R. Alcala-Orozco, J. Li, M. A. Vis, M. Santos, S. G. Wise, R. Levato, J. Malda, T. B. Woodfield, *Adv. Healthcare Mater.* **2020**, *9*, 1901667.
[35] M. McGill, J. M. Coburn, B. P. Partlow, X. Mu, D. L. Kaplan, *Acta Biomater.* **2017**, *63*, 76.
[36] B. P. Partlow, C. W. Hanna, J. Rnjak-Kovacina, J. E. Moreau, M. B. Applegate, K. A. Burke, B. Marelli, A. N. Mitropoulos, F. G. Omenetto, D. L. Kaplan, *Adv. Funct. Mater.* **2014**, *24*, 4615.
[37] J. Choi, M. McGill, N. R. Raia, O. Hasturk, D. L. Kaplan, *Adv. Healthcare Mater.* **2019**, *8*, 1900644.
[38] J. Choi, O. Hasturk, X. Mu, J. K. Sahoo, D. L. Kaplan, *Biomacromolecules* **2021**, *22*, 773.
[39] M. Castilho, R. Levato, P. N. Bernal, M. De Ruijter, C. Y. Sheng, J. Van Duijn, S. Piluso, K. Ito, J. Malda, *Biomacromolecules* **2021**, *22*, 855.
[40] P. Dorishetty, R. Balu, A. Gelmi, J. P. Mata, N. K. Dutta, N. R. Choudhury, *Biomacromolecules* **2021**, *22*, 3668.
[41] M. B. Applegate, B. P. Partlow, J. Coburn, B. Marelli, C. Pirie, R. Pineda, D. L. Kaplan, F. G. Omenetto, *Adv. Mater.* **2016**, *28*, 2417.
[42] D. Shin, J. Hyun, *J. Indus. Eng. Chem.* **2021**, *95*, 126.
[43] A. Brif, P. Laity, F. Claeyssens, C. Holland, *ACS Biomater. Sci. Eng.* **2019**, *6*, 705.
[44] F. Karimi, K. Lau, H. N. Kim, Z. Och, K. S. Lim, J. Whitelock, M. Lord, J. Rnjak-Kovacina, *ACS Appl. Mater. Interfaces* **2022**, *14*, 31551.
[45] C. S. Wyss, P. Karami, A. Demongeot, P.-E. Bourban, D. P. Pioletti, *Soft Matter* **2021**, *17*, 7038.
[46] D. N. Rockwood, R. C. Preda, T. Yücel, X. Wang, M. L. Lovett, D. L. Kaplan, *Nat. Protoc.* **2011**, *6*, 1612.
[47] P. Atienza-Roca, D. C. Kieser, X. Cui, B. Bathish, Y. Ramaswamy, G. J. Hooper, A. N. Clarkson, J. Rnjak-Kovacina, P. J. Martens, L. M. Wise, *Biomater. Sci.* **2020**, *8*, 5005.
[48] C. Guo, C. Li, D. L. Kaplan, *Biomacromolecules* **2020**, *21*, 1678.
[49] M. Ibrahim, J. Bond, M. A. Medina, L. Chen, C. Quiles, G. Kokosis, L. Bashirov, B. Klitzman, H. Levinson, *Eur. J. Plast. Surg.* **2017**, *40*, 383.
[50] S. Chen, A. F. Saeed, Q. Liu, Q. Jiang, H. Xu, G. G. Xiao, L. Rao, Y. Duo, *Signal Transduct. Targeted Ther.* **2023**, *8*, 207.
[51] C. Yunna, H. Mengru, W. Lei, C. Weidong, *Eur. J. Pharmacol.* **2020**, *877*, 173090.
[52] M. Cabeza-Cabrerizo, A. Cardoso, C. M. Minutti, M. Pereira da Costa, C. Reis e Sousa, *Annu. Rev. Immunol.* **2021**, *39*, 131.
[53] T. M. Holling, E. Schooten, P. J. van Den Elsen, *Human Immunol.* **2004**, *65*, 282.
[54] B. Chen, R. Li, A. Kubota, L. Alex, N. G. Frangogiannis, *Sci. Rep.* **2022**, *12*, 4542.
[55] O. Veiseh, J. C. Doloff, M. Ma, A. J. Vegas, H. H. Tam, A. R. Bader, J. Li, E. Langan, J. Wyckoff, W. S. Loo, *Nat. Mater.* **2015**, *14*, 643.
[56] J. Zandstra, C. Hiemstra, A. Petersen, J. Zuidema, M. Van Beuge, S. Rodriguez, A. Lathuile, G. Veldhuis, R. Steendam, R. Bank, *Eur. Cell Mater.* **2014**, *28*, 335.
[57] S. J. Shirbin, F. Karimi, N. J.-A. Chan, D. E. Heath, G. G. Qiao, *Biomacromolecules* **2016**, *17*, 2981.
[58] P. Bankhead, M. B. Loughrey, J. A. Fernández, Y. Dombrowski, D. G. McArt, P. D. Dunne, S. McQuaid, R. T. Gray, L. J. Murray, H. G. Coleman, *Sci. Rep.* **2017**, *7*, 1.
[59] C. A. Schneider, W. S. Rasband, K. W. Eliceiri, *Nat. Methods* **2012**, *9*, 671.
[60] K. J. Luebke, D. E. Carter, H. R. Garner, K. C. Brown, *J. Biomed. Mater. Res., Part A* **2004**, *68*, 696.